UNIVERSITY OF READING

Declaration of Authorship

I, JING CAO, declare that this thesis titled, `Molecular dynamics study of polymer melts' and the work presented in it are my own. I con rm that:

This work was done wholly or mainly while in candidature for a research degree at this University.

Where any part of this thesis has previously been submitted for a degree or any other quali cation at this University or any other institution, this has been clearly stated.

Where I have consulted the published work of others, this is always clearly attributed.

Where I have quoted from the work of others, the source is always given. With the exception of such quotations, this thesis is entirely my own work.

I have acknowledged all main sources of help.

Where the thesis is based on work done by myself jointly with others, I have made clear exactly what was done by others and what I have contributed myself.

Signed: _____

Date: _____

\Where there is a wiII , there is a way."

Thomas Edison

Acknowledgements

This thesis would not have been possible without the essential and gracious support of many individuals. First and foremost I o er my sincerest gratitude to my supervisor, Professor Alexei E. Likhtman, who has supported me throughout my thesis with his patience and knowledge whilst allowing me to work in my own way. Owing to his guidance, a freshman of polymer physics becomes a person who has a basic comprehension of the eld. Many thanks to Dr Zuowei Wang for reading my thesis and o ering valuable advice. Dr Jorge Ramirez and Dr Bart Vorselaars provided me many useful suggestions of computer programming, which make me work more e ciently. I also need to thank all PhD students in our group, Mohamad Shukor Talib, Tim Palmer, Tom Beardsley, who always have a relaxing chat on physical and non-physical problems. Also thanks Katrina Likhtman to provide homey parties and delicious food. Finally, I thank my parents for supporting me throughout all my studies abroad and never enough thanks to my girl friend, Lei Wang, for listening and supporting.

Contents

List of Figures

:i5.i29ii -1.790fF16=10.9552 Tf 3.252 0 Td [(2)

List of Tables

Abbreviations

SDE	Stochastic Di erential Equation
RDF	Radial Distribution Function
CLF	Contour Length Fluctuation
CR	Constraint Release
VPF	Vacuum Projection Force
PY	Percus-Yevick
HNC	HyperNetted Chain

Symbols

G	stress relaxation modulus	
R	monomer position vector	
r	bond vector	
T	temperature	^oC
m	mass	kg
t	time	s
U	potential	kg m^2=s^2
	stress tensor	N m ^{2}
	strain	
	viscosity	Pa s
	friction coe cient	N s=m
_	shear rate	s ^{1}
W	Wiesenberg nmber(_)	

To my family

Chapter 1

1.2 Microscopic de nition of stress

As we known, force can be exerted externally on a body in two particular ways. The gravity and inertia can be thought of as *body forces* since they act directly on all individual particles in the body. The other type are *surface forces* which act only on the surface of a body, but their e ect is transmitted to the particles inside the body through the atomic and molecular bonds. In order to de ne the state of stress at a point within the body we consider the surface forces acting on a small cube of material around that point. We de ne the **stress** as the ratio of the force and the cross-sectional area. Both the force and the cross-sectional area have direction and magnitude(the direction of the cross-sectional area being described by its normal unit vector), which make the stress a tensor. The - component of the **stress tensor** is the force applied in the direction per unit of the cross-sectional area of a network perpendicular to the axis from outside. In most material the stress tensor is symmetric. We will only consider symmetric stress tensors in this thesis.

$$= \begin{pmatrix} xx & xy & xz \\ xy & yy & yz \\ xz & yz & zz \end{pmatrix} \tag{1.3}$$

In the consideration of the mechanical properties of the polymers, it is useful to divide the stress tensor into its hydrostatic and deviatoric components. The hydrostatic pressure p is given by

$$p = \frac{1}{3}(xx + yy + zz) \tag{1.4}$$

and the deviatoric stress tensor $'$ is found by subtracting the hydrostatic stress components from the overall tensor such that

$$' = \begin{pmatrix} (xx \quad p) & xy & xz \\ xy & (yy \quad p) & yz \\ xz & yz & (zz \quad p) \end{pmatrix} \tag{1.5}$$

The rheological constitutive equations make the predictions of the stress tensor
. Now we would like to know how to derive the stress of the system from the

Chapter 1.

The simplest model of viscoelasticity is the Maxwell model[1], which combines a perfectly elastic element with a perfectly viscous element in series. Since the elements are in series, the total shear strain is the sum of the shear strain in each element $= {}_e + {}_v$, both of the elements must bear the same stress $= G\ {}_e = \frac{d\ {}_v}{dt}$. The ratio of the viscosity and the modulus G de nes characteristic time scale, called the relaxation time $= =G$.

1.5.2 Stress relaxation after a step strain

When a step strain was applied at time $t = 0$, the stress relaxation modulus $G(t)$ is de ned as the ratio of the stress remaining at time t and the magnitude of this step strain : $G(t) = (t)= $. For viscoelastic solids, $G(t)$ relaxes to a nite value, called the equilibrium shear modulus $G_{eq} = \lim_{t\ !\ 1} G(t)$. For viscoelastic liquids, the Maxwell model can be used to understand the stress relaxation modulus. After solving a rst order di erential equation of the time-dependent strain in the viscous element, the stress relaxation modulus in this case has a simple exponential decay:

$$G(t) = \frac{(t)}{} = G_0 \exp(\ \ t=) \tag{1.10}$$

The relaxation time is a fundamental dynamic property of all viscoelastic liquids. Polymer liquids normally have multiple relaxation modes, each with its own relaxation time. Any stress relaxation modulus can be described by a combination of serial Maxwell elements. Most materials have a region of linear response at su ciently small values of applied strain, where the relaxation modulus is independent of strain.

If the applied shear rate is too large for linear response, Boltzmann superposition no longer holds. Most polymeric liquids exhibit shear thinning of the apparent viscosity at large shear rates, which means that the viscosity decreases with increasing the shear rate. The apparent viscosity has also been observed to increase with the shear rate increase for some materials, which is called shear thickening.

1.5.5 Oscillatory shear

In practice, the simplest linear viscoelastic measurement is oscillatory shear[2]. A harmonic oscillation of strain with angular frequency $!$ is applied to a sample in simple shear: $(t) = {}_0\cos(! t)$. The principal advantage of this technique is that the viscoelastic response of any material can be probed directly on di erent time scale of interest $t \quad 1=!$ by varying the angular frequency $!$. If the material studied is a perfectly elastic solid, then the stress in the sample will be related to the strain through Hooke's law:

$$(t) = G_0 \ {}_0\cos(! t):$$

By using Boltzmann superposition integral(Eq.1.12),

$$\begin{aligned}
(!;t) &= \int_{-\infty}^{t} G(t-t')\dot{\gamma}(t')dt' \\
&= \int_{-\infty}^{t} G(t-t')\gamma_0 ! \sin(!t')dt' \\
&= Re\int_{-\infty}^{t} G(t-t')\gamma_0 i! \exp(i!t')dt' \\
&= Re[\gamma_0 G^*(!)\exp(i!t)] \qquad (1.18)
\end{aligned}$$

where the complex modulus $G^*(!)$ is de ned by:

$$G^*(!) = i!\int_0^{1} G(t)\exp(-i!t)dt \qquad (1.19)$$

The form of Eq.(1.18) means that the stress will also be oscillatory at frequency $!$, but not in phase with the strain. If we write $G^*(!) = G'(!) + iG''(!)$, then we can identify the real part G', called the storage modulus, as the in-phase part of the modulus and the imaginary part G'', called loss modulus, as the out-of-phase part. Assume $G(t) \to 0$ as $t \to +\infty$.

$$G'(!) = !\int_0^{\infty} G(t)\sin(!t)dt \qquad (1.20)$$

$$G''(!) = !\int_0^{\infty} G(t)\cos(!t)dt \qquad (1.21)$$

In general both will be frequency-dependent, crossing over from viscous behavior at low frequencies to elastic behavior at high frequencies. Then Eq.(1.18) can be written as following:

$$\begin{aligned}
(!;t) &= Re[\gamma_0 G^*(!)\exp(i!t)] \\
&= Re[\gamma_0(G'(!) + iG''(!))(\cos(!t) + i\sin(!t))] \\
&= \gamma_0(G'(!)\cos(!t) - G''(!)\sin(!t)) \qquad (1.22)
\end{aligned}$$

According to Eq.(1.17) and Eq.(1.22), the ideal Newtonian uids have a shear stress that is simply proportional to the current shear rate.

$$(t) = \frac{@}{@t} = Re[\ i! \ _0 \exp(i!t)]\ ) \begin{cases} G'(!) = 0 \\ G''(!) = \ ! \end{cases} \tag{1.23}$$

At the opposite material extreme, the ideal elastic solids have a shear stress that is simply proportional to the current shear strain.

$$(t) = G_0 \ = G_0 \ _0 Re[\exp(i!t)]\ ) \begin{cases} G'(!) = G_0 \\ G''(!) = 0 \end{cases} \tag{1.24}$$

For the single Maxwell model of a2(or)-67s1(ell)-Td [50

of the Brownian particles are governed by Newton's law: $f = ma = m\ddot{r}$, where a is the acceleration vector of the particle. f represents the forces acting on the particle, which can be divided in random force f_R and friction force f_F. Note that now the Brownian motion term is used to describe the random motion of molecules and atoms as well.

1.6.1 Random force

The random force f_R acting on a particle is due to many collisions with the other molecules surrounding it. The collisions take place very fast and are unpredictable in nature, so we will consider each of them, f_{Ri}, to take place in a random direction

have

$$f_F = \quad v = \quad \frac{dr}{dt} \tag{1.26}$$

1.6.3 Fluctuation-dissipation theorem

Consider a time-dependent external field $h(t)$ is applied to a system in equilibrium. A physical observable A is called conjugate to the field h if the change of Hamiltonian due to the field h can be written as $H = hA$. If the field is weak,

On the other hand, if we apply a sudden step field on an equilibrium system at $t = 0$, Eq.(1.27) turns into

$$\langle A(t)\rangle_h - \langle A_0\rangle = h \int_0^t \quad (t')dt' \tag{1.31}$$

From Eqs.(1.28) and (1.31), we can derive

$$\langle A(t)\rangle_h - \langle A_0\rangle = \frac{h}{k_B T}(C_{AA}(0) - C_{AA}(t)) \tag{1.32}$$

$$= \frac{h}{2k_B T}h(A(t) - A(0))^2 i \tag{1.33}$$

The fluctuation-dissipation theorem connects the relaxation from a non-equilibrium state, which is not far from the equilibrium state, i.e. in linear regime, with the spontaneous microscopic dynamics in the equilibrium system.

So far, we have the following expression for the forces acting on the Brownian particles:

$$f(t)dt = (f_R(t) + f_F(t))dt = - dW - dr \tag{1.34}$$

It is usual to work in the limit of strong friction where inertia term $m\ddot{r}$ can be

Figure 1.3: Relationship between friction and random forces

From Eq.(1.33) and the property of Wiener process in one-dimension $\langle(dr)^2\rangle = 2D\,dt$ where dr is the displacement of the particle during dt and D is the diffusion coefficient, the following equation can be derived using h

where is the friction coe cient, m is the monomer mass, $U(\{R_i\})$ is the intra-chain interaction potential, and W_i is a Wiener process for particle i.

1.7 Gaussian chains

1.7.1 Gaussian chain model

In the Gaussian chain model, we forget about the local details of the chain, and assume that every bond r_i is actually the sum of many bond vectors, so that the probability distribution of r_i is Gaussian. The assumption is that the di erent bonds along the chain are independent of each other, $\langle r_i \cdot r_j \rangle = \langle r_i \rangle \cdot \langle r_j \rangle$ if $i \neq j$. The bond length is not constant. Each bond is exible and follows a Gaussian distribution:

$$p(r) = \left(\frac{3}{2\pi b^2}\right)^{\frac{3}{2}} \exp\left(-\frac{3r^2}{2b^2}\right) \tag{1.41}$$

with $\langle r \rangle = 0$ and $\langle r^2 \rangle = b^2$. The probability distribution of a given conformation $\{r_i\} = \{r_1, \ldots, r_N\}$ is:

$$\Psi(\{r_i\}) = \prod_{i=1}^{N} p(r_i) = \left(\frac{3}{2\pi b^2}\right)^{\frac{3N}{2}} \exp\left(-\frac{3}{2b^2}\sum_{i=1}^{N} r_i^2\right) \tag{1.42}$$

It has an important property that the distribution function of the vector between any two beads of the Gaussian chain is also Gaussian with $\langle R_i - R_j \rangle = 0$ and $\langle (R_i - R_j)^2 \rangle = |i - j| b^2$.

$$p(R_i - R_j) = \left(\frac{3}{2\pi b^2 |i-j|}\right)^{\frac{3}{2}} \exp\left(-\frac{3(R_i - R_j)^2}{2|i-j|b^2}\right) \tag{1.43}$$

In Eq.(1.43), if we set $i = N$ and $j = 0$, the equation turns into

$$p(R_N - R_0) = p(R_e) = \left(\frac{3}{2\pi N b^2}\right)^{\frac{3}{2}} \exp\left(-\frac{3R_e^2}{2Nb^2}\right) \tag{1.44}$$

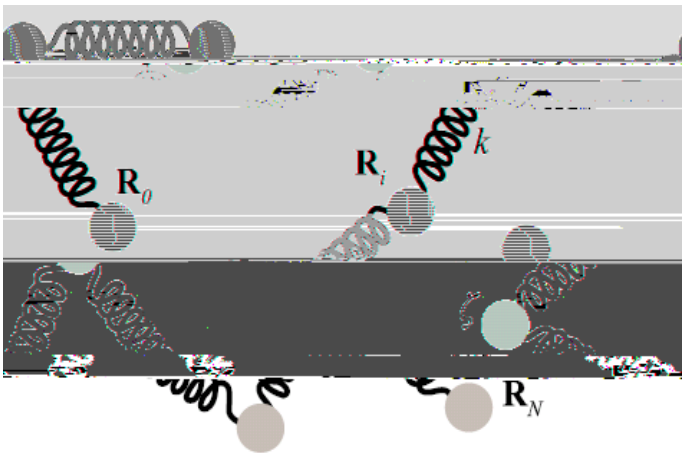

Figure 1.5: Rouse model for polymers.

1.7.3 Rouse model

Rouse model, which is a cornerstone of polymer dynamics, was originally proposed by Rouse[4] in 1953. The model is treated as a collection of $N+1$ beads connected by harmonic springs(Fig.1.5), which is de ned by the equation of motion Eq.(1.40) without inertia with the simplest possible potential

$$U(\{R_i\}) = \frac{3k_BT}{2b^2}\sum_{i=0}^{N-1}(R_{i+1} - R_i) \tag{1.45}$$

Each bead is characterized by its own independent friction force with the friction coe cient . The total friction coe cient of the whole Rouse chain is the sum of the contributions of each of the $N+1$ beads: $_{chain} = (N+1)$. We can write the stochastic di erential equation for each bead along the chain:

$$dR_0 = \frac{3k_BT}{b^2}(R_1 - R_0)dt + \sqrt{2k_BT}\,dW_{t0} \tag{1.46}$$

$$\vdots = \vdots$$

$$dR_i = \frac{3k_BT}{b^2}(R_{i+1} + R_{i-1} - 2R_i)dt + \sqrt{2k_BT}\,dW_{ti} \tag{1.47}$$

$$\vdots = \vdots$$

$$dR_N = \frac{3k_BT}{b^2}(R_{N-1} - R_N)dt + \sqrt{2k_BT}\,dW_{tN} \tag{1.48}$$

where W_{ti} is a vector Wiener processes in terms of the bead number i:

$$\begin{aligned} \langle W_{ti} \rangle &= 0 \\ \langle W_{ti} \, W_{t'j} \rangle &= \delta_{ij} \min(t; t') \end{aligned}$$

Figure 1.6: The tube model

chain to move freely along its own contour length but not perpendicular to its contour(Fig.1.6). A piece of chain which escaped from the tube is assumed to adopt a random orientation independent of surrounding chains. Merrill *et al.*[9]

1.8.1 Primitive chain

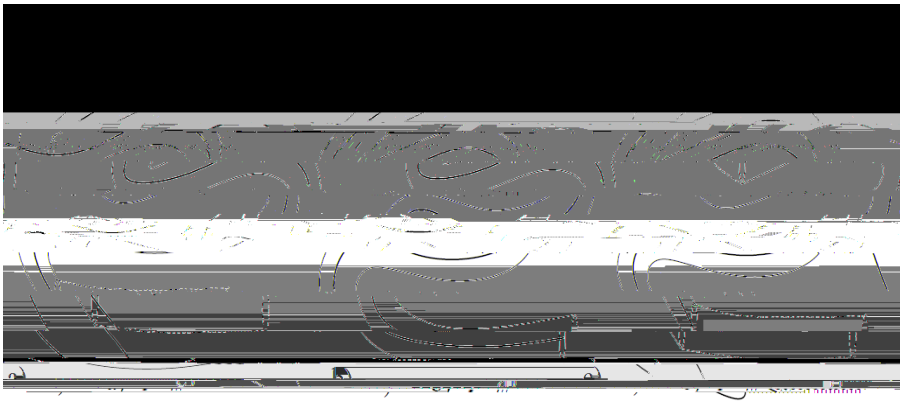

Figure 1.7: The relaxation of the primitive chain.

1.8.2 Reptation

Now we can study the dynamics of the primitive chain. In the beginning, the original primitive chain is trapped in a tube like region(Fig.1.7(*a*)). After the primitive chain moves along the contour length back and forward, which is called reptation, one end of the chain escapes from the original tube and can adopt any directions, the other end of the tube disappears as it is evacuated (dashed line in Fig.1.7(*b*)). As the chain moves back and forward on both directions, the tube is destroyed from both ends(Fig.1.7(*c*)). The time correlation function of the end-to-end vector $R_e(t) = R(L;t) \quad R(0;t)$ is given by

$$hR_e(t) \quad R_e(0)i = Nb^2 \sum_{p=odd} \frac{8}{p^2 \ ^2} \exp(\quad \frac{p^2 t}{d}) \tag{1.56}$$

The time $_d$ is known as the reptation time and is related to the molecular parameters by

$$_d = \frac{N^3 b^4}{^2 k_B T a^2} = 3Z \ _R: \tag{1.57}$$

From Eq.(1.56), we can see that the time correlation function of the end-to-end vector is dominated by the rst term with $p = 1$.

We can introduce a mathematical equation for reptation dynamics:

$$R(s;t + \quad t) = R(s + \quad s(t);t) \tag{1.58}$$

where $s(t)$ is the distance that the primitive chain moves in a time interval t and it is a Gaussian random variable with

$$\langle s(t) \rangle = 0 \tag{1.59}$$

$$\langle s(t)^2 \rangle = 2D_c t \tag{1.60}$$

But if $s + s(t)$ is not between 0 and L, $R(s; t + t)$ should be on a new tube segment.

Now we can calculate the mean-square displacement $\langle (R(s;t) - R(s;0))^2 \rangle$ of the primitive chain segment s. The function $'(s; s^0; t)$ is de ned as following:

$$'(s; s^0; t) = \langle (R(s;t) - R(s^0;0))^2 \rangle \tag{1.61}$$

The time evolution equation of $'(s; s^0; t)$ is

$$\begin{aligned} '(s; s^0; t + t) &= \langle (R(s; t + t) - R(s^0; 0))^2 \rangle \\ &= \langle (R(s + s(t); t) - R(s^0; 0))^2 \rangle && (1.62) \\ &= \langle '(s + s(t); s^0; t) \rangle && (1.63) \\ &= \left(1 + s\frac{@}{@s} + \frac{s^2}{2}\frac{@^2}{@s^2}\right) '(s; s^0; t) && (1.64) \\ &= \left(1 + \langle s \rangle \frac{@}{@s} + \frac{\langle s^2 \rangle}{2}\frac{@^2}{@s^2}\right) '(s; s^0; t) && (1.65) \end{aligned}$$

And then we can get the equation

$$\frac{@}{@t} '(s; s^0; t) = D_c \frac{@^2}{@s^2} '(s; s^0; t) \tag{1.66}$$

The initial condition is

$$'(s; s^0; t)|_{t=0} = |s - s^0|. \tag{1.67}$$

The boundary conditions are

$$\left.\frac{@ '(s; s^0; t)}{@s}\right|_{s=0} = a; \qquad \left.\frac{@ '(s; s^0; t)}{@s}\right|_{s=L} = a. \tag{1.68}$$

From the calculation of Doi *et al.*[1], the solution of Eq.(1.66) is

$$'(s;s^{0};t) = js \quad s^{0}ja + \frac{2aD_c t}{L} + \sum_{p=1}^{\infty} \frac{4La}{p^2\ ^2}\cos\ \frac{p\ s}{L}\ \cos\ \frac{p\ s^{0}}{L}\ (1 \quad \exp(\ \ tp^2=\ _d)) \tag{1.69}$$

For t $_d$, $'(s;s;t)$ is dominated by the terms with large p.

$$'(s;s;t) \quad 2a\sqrt{D_c t=} \tag{1.70}$$

For $t >$ $_d$, $'(s;s;t)$ is dominated by the terms with $p = 1$.

$$'(s;s;t) \quad 2D_c t=Z \tag{1.71}$$

1.8.3 Contour length uctuation(CLF)

In previous sections, the primitive chain was regarded as an inextensible string of contour length L. In reality, the contour length of the primitive path ought to be continually uctuating around its equilibrium length under the in uence of thermal uctuations, and uctuations sometimes play an important role in various dynamical properties. Since the primitive chain represents a set of conformations of the Rouse chain, the probability of a certain conformation of the primitive chain is proportional to the number of the conformation of the Rouse chain which can be represented by that primitive chain. If we set the polymer as a random walk con ned in a tube, the entropy of the primitive chain was calculated as following[1]:

$$S(L) = S_0 \quad k_B \quad \frac{3L^2}{2Nb^2} + \ _0\frac{Nb^2}{a^2} \tag{1.72}$$

where S_0

simulations of polymer melts, one has to minimize the nite size e ects by using periodic boundary condition.

1.9.1 Periodic boundary condition

Todd and Daivis[11] indicated the e ects of periodic boundary condition on the calculation of the stress tensor of the system. If the number of the particles in the system and the volume are nite, the stress tensor can be calculated as following:

$$(t) = \frac{1}{V} \sum_{i=1}^{N} R_i(t) f_i(t) \tag{1.73}$$

or

$$(t) = \frac{1}{2V} \sum_{i=1}^{N} \sum_{j \neq i}^{N} r_{ij} f_{ij} \tag{1.74}$$

where ; are Cartesian coordinates, V is the volume of the system, N is the number of particles in the system, R_i is the position vector of particle i, f_i is the force on particle i, r_{ij} and f_{ij} are the distance vector and force from particle j to i respectively. However the volume of the system is in nite under periodic boundary condition. If we map all the particles into a periodic box, the volume is nite. But Eq.(1.73

where the spring constant $k = 30''= {}^2$ and the maximum bond length $R_{max} = 1{:}5$, at which the elastic energy of the bond becomes in nite. The combination of U_{LJ} and U_{FENE} leads to an average bond length $hl^2 i^{1=2}$ 0:97 . In addition, a harmonic bending potential is used to introduce some sti ness into the polymer chain.

$$U_{bend} = \frac{k_b}{2} \sum_{i=1}^{N} (R_{i+1} \quad 2R_i + R_{i\ 1})^2 \tag{1.78}$$

where R_i is the position vector of ith monomer in the chain. In this way the forces are pairwise and the bending force on the monomer i is

$$f^i_{bend} = 4k_b(R_{i+1} + R_{i\ 1} \quad 2R_i) \quad k_b(R_{i+2} + R_{i\ 2} \quad 2R_i)$$

Thus, our bending potential corresponds to an attractive harmonic spring $4k_b$ between the neighbouring monomers and a repulsive harmonic spring k_b between monomers with chemical distance 2.

1.9.3 Equations of motion

The velocity Verlet algorithm is used to integrate the equations of motion of the monomers. The system is coupled to a Langevin thermostat by the standard equation,

$$m\ddot{r}_i = \quad r_i U(fr_i g) \quad \underline{r}_i + f_i; \tag{1.79}$$

where m is the monomers mass and is the friction coe cient set to be $0{:}5(mk_B T)^{1=2}= $. The stochastic force f_i is given by a -correlated Gaussian noise source. The friction constant and Langevin noise term f_i are introduced to control the temperature and to stabilize the system. They are related by the uctuation-dissipation theorem as $hf_i(t) \quad f_i(t^0)i = 6k_B T \quad (t \quad t^0)$.

1.9.4 Other parameters

The simulations are performed with periodic boundary conditions applied in all three dimensions of the cubic simulation box. The time step $t = 0.012$ is used in all simulation runs, where $= (m\ ^2/k_B T)^{1/2}$ is the LJ time unit. The usual simulations of melts are carried out at a temperature $T = "/k_B$ and monomer number density $= 0.85\ ^3$.

1.10 Motivation

The rheology of linear monodisperse polymers in equilibrium is the fundamental

of their creation and destruction. Microscopic molecular dynamics simulations are a feasible way to derive these parameters. The shear simulation is also an intermediate step between the experiments and the simple models. We will discuss the non-equilibrium study in Chapter 3, developing basic methods to produce non-linear rheology data from MD simulations.

As discussed before the molecular dynamics simulations are used as an experimental tool to understand the behaviour of polymer melts. Due to the limit of computer power and the large number of particles, we can not simulate a real sample at the molecular level. This encourages us to use di erent models at di erent scaling levels, which is also called coarse-grained simulations. The advantage of this method is that if we are only interested in the macroscopic properties of the polymer, the same result can be derived by using corresponding coarse-grained simulations correctly with less variables of the system and shorter simulation times. In chapter 4, we aim to derive coarse-grained variables from microscopic simulations in a systematic way and reproduce some quantities in microscopic simulations by using these variables.

Chapter 2

Orientational relaxation and coupling in equilibrium polymer melts

2.1 Overview

Slow relaxation in polymer melts has attracted constant attention of theoreticians for the last 40 years, perhaps partly because it is still lacking a general framework description. Indeed, melts of short chains are called unentangled and described by the Rouse theory[4]. Relaxation in melts of longer chains is believed to be dominated by entanglements, and is consequently described by the tube theory[14][1], which is a mean eld description of an entangled system. Based on the tube theory, the terminal relaxation time $_d$ and the zero shear viscosity $_0$ are proportional to the cube of the molecular weight M_w in monodisperse melts. Although experimental data show a slightly larger exponent around 3:4, the tube theory has been regarded as a theoretical triumph. Many modi cations like contour length uctuation(CLF)[10][15] and constrai0 G4os15(b)273

the entanglement segments. Likhtman and McLeish[17] improved the treatment of contour length fluctuations using a combined theoretical and stochastic simulation approach which allows them to obtain an expression for the single chain relaxation function (t) without any adjustable parameters and approximations. They then used the scheme proposed by Rubinstein and Colby[16], which provides an algorithm for calculating the full relaxation function $G(t)$ from the single chain relaxation (t), to include the constraint release mechanism. They produced excellent agreement between theory and experiment in the linear regime. All these mechanisms from monodisperse melts should be involved in the study of polydisperse melts, which would include several other mechanisms.

In order to understand the rheology of polydisperse melts, a simple case of mixtures of long and short chains should be investigated first. The concept of CR becomes very useful and important for binary blends. After the terminal relaxation time of the short component, short chains move away and release their constraint on the long probe chain. The entanglements left in the system are the ones between the long chains. Then a dilated tube constructed by other long chains can be introduced. However, the tube dilation was not found useful in entangled linear monodisperse melts although it was applied to describe the dynamics of branched polymers successfully[19][20]. Following the initial idea of Marrucci[21], Doi *et al.*[22] derived the condition under which the long component in a binary blend would reptate in a dilated tube. They concluded that the relaxation of a long chain in binary blend would not be faster than the relaxation in the pure long chain melt if the Struglinski-Graessley parameter $r_{SG} = N_l N_e^2 / N_s^3$ is smaller than one. When $r_{SG} > 1$, Doi *et al.* suggested that the long chain would reptate in the

r_{SG}

chosen to be smaller than the entangled length N_e to avoid the complication associated with the entanglements between long and short chains. They also studied the homo-mixture of long and short chains of polybutadiene, in which the short chains were longer than the entangled length N_e[26]. In binary blends with a Struglinski-Graessley parameter smaller than one, they saw a discernable shift of the terminal relaxation time with the composition, which contradicts the previous theories of Viovy *et al.*[27] and Doi *et al.*[22].

Wang *et al.*[28] presented extensive molecular dynamics simulations of the dynamics of diluted long probe chains entangled with a matrix of short chains. The constraint release effect in the binary blends was investigated by systematically reducing the short chain length N_s from the monodisperse case of $N_s = N_l$ to slightly above one entanglement length. The diffusion of the long chains, measured by the mean square displacements of the monomers and the centers of mass of the chains, demonstrated a systematic speed-up relative to the pure reptation behavior expected for monodisperse melts of sufficiently long polymers. On the other hand, the diffusion of the matrix chains was only weakly perturbed by the diluted long probe chains.

The aim of this chapter is to investigate the stress and orientation relaxation of monodisperse and bidisperse melts in both unentangled and mildly entangled systems, and to find out how the dynamics of each component are affected by the composition of the system. In section 2.2, we will introduce the definition of stress and orientation relaxation functions and cross-correlation functions used in this thesis. In section 2.3, the stress-optical rule in MD simulations is established. In sections 2.4 and 2.5, the stress and orientational relaxation of monodisperse and bidisperse melts are investigated respectively. In section 2.6, we will propose a universal time-dependent orientational coupling parameter for both monodisperse and bidisperse melts. Using this universal coupling parameter, the total relaxation function of binary blends can be obtained from the auto-relaxation function of each component.

Chapter 2.

Chapter 2.

functions of two monodisperse melts and of their 50% blend, together with orientation relaxation, multiplied by 1= . We found that = 0:0885 and 1:28 for exible and semi- exible Kremer-Grest model at monomer density =0:85 ^{3} respectively. Three important observations are due: (i) indeed the two relaxation functions become proportional to each other after about 30 Lennard-Jones time units, and remain proportional to each other with accuracy better than 1%; (ii) The stress-optical coe cient does not depend on chain lengths and (iii) it remains the same for binary blends, in accordance with experiment. In Fig.2.2 we plot the stress-optical coe cient times density as a function of density in both exible and semi- exible systems. The curve from exible system is shifted upward by a factor of 10 to compare with the ones from semi- exible system. We can see that the results behave di erently in two systems. Thus, studying orientation coupling should provide useful information for the stress relaxation and rheology.

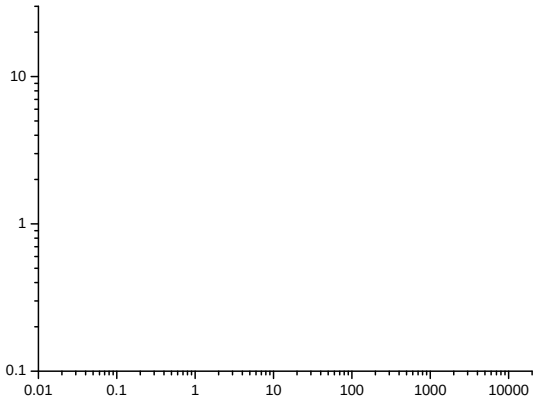

Figure 2.3: Mean-square displacement of chain ends and middle for exible chains.

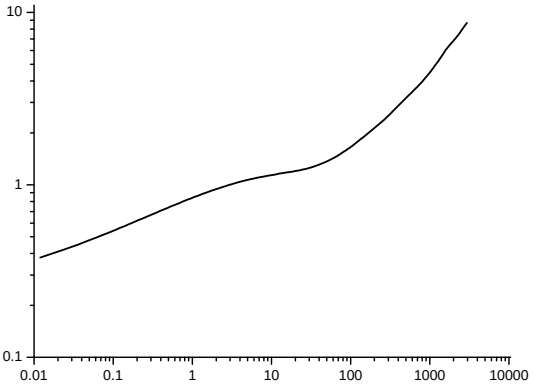

Figure 2.4: Mean-square displacement of chain ends and middle for semi- exible chains.

the random walk in the space and do not feel the connectivity at these short times. Then the plateaus come out for both middle and end monomers which indicates that the chains are in Rouse regime. After comparing the maximum for middle and end monomers, we can see that the mean-square displacement of chain ends is exactly twice of counterpart of middle section, which can be explained by that the chain ends only feel the connectivity from one side comparing to from both sides for middle monomers. Now the curves of entangled systems deviate from the ones of unentangled systems. A negative slope around 1=4 comes out in entangled systems which indicates that the chain is trapped in a constraint tube and reptation and CLF are the only mechanisms in this regime. After the time when chains are totally relaxed, two curves of middle and ends monomers join each other and have a positive slope around 0:5 which can be interpreted as the escape time from the tube.

2.4.2 Storage and loss moduli

We rst present the storage and loss moduli in exible and semi- exible monodisperse melts with di erent chain lengths in Fig.2.5-2.8. The terminal time and zero-shear viscosity of di erent chain lengths and sti nesses are listed in Table.2.1. The entanglement lengths N_e of exible and semi- exible chains are around 50 and 15 respectively[30]. From Fig.2.5 and Fig.2.7, $G^0(!)$ starts to show a plateau with

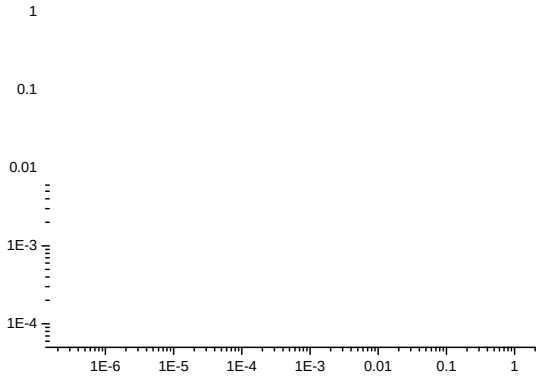

Figure 2.5: G' of monodisperse melts of flexible chains.

Figure 2.6: G'' of monodisperse melts of flexible chains.

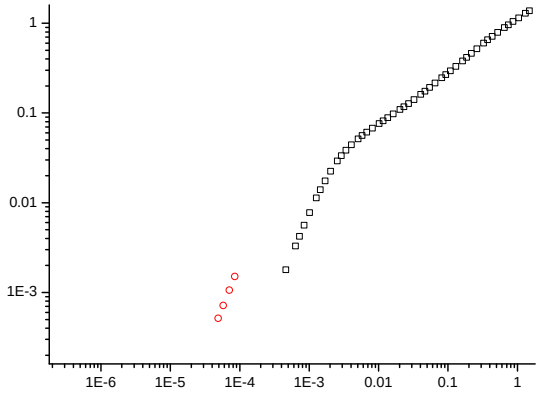

Figure 2.7: G' of monodisperse melts of semi- flexible chains.

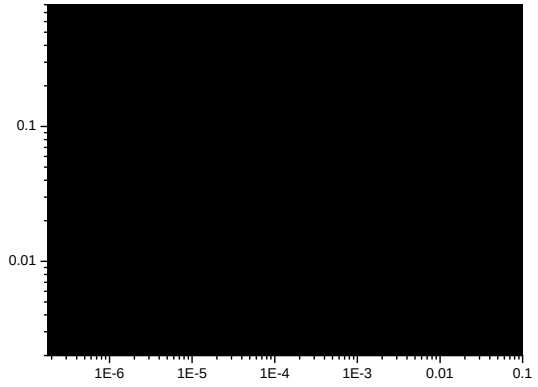

Figure 2.8: G'' of monodisperse melts of semi- flexible chains.

increasing chain length. After comparing these two figures, $G'(\omega)$ behaves similar if two chains with different stiffnesses have the same number of entanglements. i.e. flexible chain with $N=256$ and semi- flexible chain with $N=75$ both have around 5 entanglements. However, $G''(\omega)$ have different features with different stiffness even if both chains have same number of entanglements. The modulus G_c at the crossing point is defined as

$$G_c = G'(\omega_c) = G''(\omega_c) \quad G''_{max}.$$

In the semi- flexible systems, the amplitude of G''_{max} is almost the same for different chain lengths which is not true in flexible systems.

2.4.3 Orientational relaxation

In order to investigate relaxation coupling between di erent chains, the total and self orientational relaxation functions of monodisperse melts are measured in ex- ible and semi- exible systems. The lines and open symbols in Fig.2.9 and Fig.2.10 are the total relaxation functions $S(t)$ and the self relaxation functions $A(t)$ re- spectively. We use several Maxwell modes to t the self relaxation functions $A(t)$

$$A(t) = \sum_i G_i \exp(\quad t= \ _i) \tag{2.18}$$

where G_i and $\ _i$ are the plateau modulus and relaxation time of mode i. The terminal relaxation time $\ _d$ is the largest $\ _i$ among all the modes. We can see that the terminal time $\ _d$ becomes larger with increasing chain length(Table.2.1). The ratio of $\ _d$ and the square of molecular weight are shown in Fig.2.11. As the molecular weight of one entanglement strand N_e in exible and semi- exible systems are 50 and 15 respectively, we can see that the data for exible chains in Fig.2.11 remains constant when N<100 which obey the Rouse theory($\ _d \quad N^2$) and then a slope of 1 comes out when N=256. The semi- exible data points presented well entangled systems which obey the reptation theory($\ _d \quad N^3$). However, it seems that the last points in both systems did not follow the reptation theory. We suppose the reason is that the simulation time is not long enough to obtain accurate data for such long chains.

Flexible($k_b = 0$)	Semi- exible($k_b = 3$)

$= 1.05^{3}$. This is because the monomers are trapped in \cages" created by other surrounding monomers and spend more times in them before escape, and the bonds are a ected in a similar way. Now we are going to ask what will happen if two components with di erent chain lengths are mixed. Ylitalo *et al.*[31] have shown that the concentration of the short component will strongly a ect the relaxation of the long component. Now we would like to investigate how the composition of binary blends a ect the dynamics of each component.

2.5 Bidisperse melts

2.5.1 Monomer mean-square displacement

In this section, we will investigate the mean-square displacement of monomers of each component in semi- exible binary blends. In Fig.2.13, short and long components have chain lengths $N_1 = 30$; $N_2 = 150$ which are shown by lines and symbols respectively. Di erent colours indicate di erent composition of binary blends. Similar features are observed comparing to the mean-square displacement of monodisperse melts(Fig.2.4). The dynamics of short chains feels little e ect from the composition of the blend. However, the long chains' properties change

Figure 2.13: Mean-square displacement of short(lines) and long(symbols) components in semi- exible binary blends of N_1=30; N_2=150.

Figure 2.14: Mean-square displacement of long chains in semi- exible binary blends with N_2 = 150; $'_l$=90%.

the $g_1(t)$ of long component. In Fig.2.14, the length of long component is N_2=150, the lengths of short component are chosen as 30 and 75. The volume fraction of long chains $'_l$ is set to 90%. We can see that the mean-square displacement of middle and end section of long component overlap with each other.

2.5.2 Storage and loss moduli of semi- exible chains

In this section we will concentrate on the relaxation functions of binary blends. Because the entanglement length N_e is much larger in exible system than in the semi- exible system, the chain length would be much longer in exible system if the same number of entanglements is required. So we will only investigate the semi- exible binary blends in this section. N_1=3; 15; 30; 75 and N_2=150 are chosen for the short and long components respectively.

First the binary blend of N_1=30; N_2=150 will be investigated, whose components have big di erence of terminal relaxation time. G' and G'' of the binary blends with di erent compositions are shown in Fig.2.15 and Fig.2.16 together with monodisperse melts of each component. In Fig.2.15, G' has two clear relaxation steps in the blends with $'_l$=10%; 30%. G'' in Fig.2.16 shows more interesting

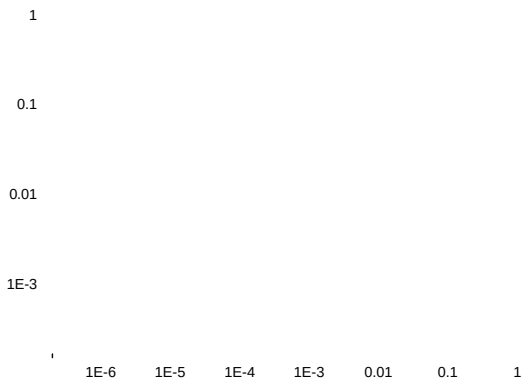

Figure 2.15: *G*

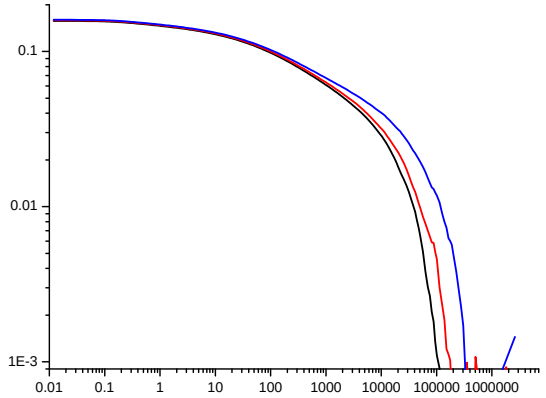

Figure 2.21: Total orientational relaxation function in binary blends of flexible chains for different compositions.

Figure 2.22: Total orientational relaxation function in binary blends of semi-flexible chains for different compositions.

chain. However, at longer times total relaxation is governed only by the long chains' relaxation as indicated by the shape of the relaxation functions. The terminal relaxation of the whole system is controlled by the slowest relaxing component in the blends.

Now we turn our attention to different contributions to the total relaxation function. All six terms in Eq.(2.15) of flexible and semi-flexible systems are shown in Fig.2.23 and Fig.2.24 respectively. Surprisingly, the cross-correlation function between short and long components does not relax until the relaxation time of the long chains, which indicates that the coupling is an important relaxation mechanism at all times. We can also see that $C_{ss}(t)$ is not totally relaxed after the terminal relaxation time of the short component. It is possibly a result of two short chains being coupled with long chains at the same time, which makes both short chains affected by

into

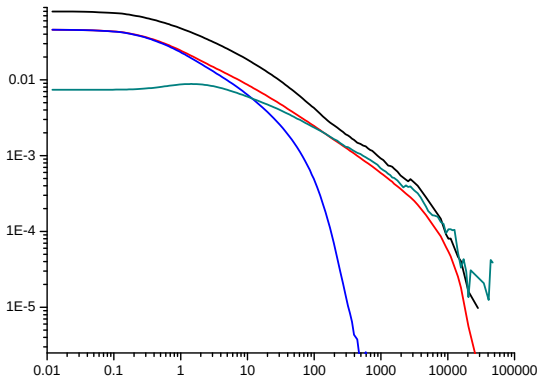

Figure 2.23: All components of orientation relaxation function of binary blend of exible chains.

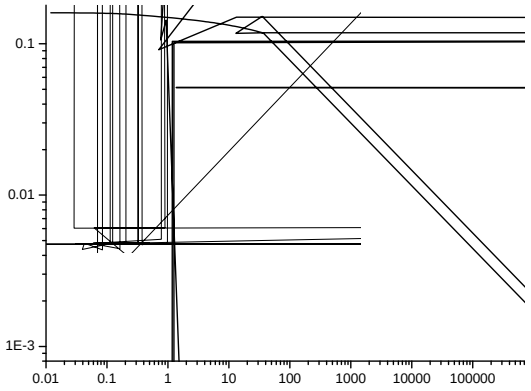

Figure 2.24: All components of orientation relaxation function of binary blend of semi- exible chains.

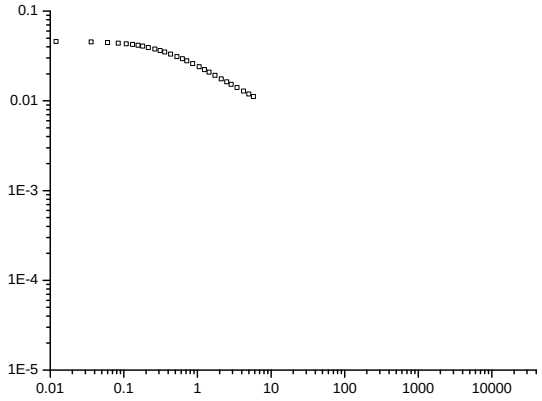

Figure 2.25: $A_s(t)$(symbols) and $E_s(t)$(lines) of short chains. Di erent colours are for di erent concentrations of the long chains.

Figure 2.26: $A_l(t)$(symbols) and $E_l(t)$(lines) of long chains. Di erent colours are for di erent concentrations of the long chains.

terms:

$$E_s(t) = A_s(t) + {}'_s C_{ss}(t) + {}'_l C_{sl}(t) \quad (2.19)$$

$$E_l(t) = A_l(t) + {}'_l C_{ll}(t) + {}'_s C_{sl}(t) \quad (2.20)$$

Summing up these two equations we can see that $S_{tot}(t) = {}'_s E_s(t) + {}'_l E_l(t)$.

Relaxation functions of short component in exible systems are presented in Fig.2.25 together with its auto-correlation function. In these gures, the e ect of long chains in the system is surprisingly strong, producing a dramatic retardation in the short component relaxation with increasing concentration of long chains. After comparing Fig.2.21 and Fig.2.25, we can see that the terminal relaxation

on large scales, making single chain dynamics Rouse-like at large scales. However, the fact that each individual chain obeys Rouse dynamics does not mean that the total stress relaxation is also known: this will only be true if cross-correlation between the chains are negligible, which as we showed in Figs.2.21-2.24 is clearly not the case.

The tube theory uses an assumption of chain independence twice: each chain reptates in its tube independently, and the piece of chain which escaped from the tube is assumed to adopt a random orientation independent on surrounding chains. Merrill *et al.*[9] demonstrated a long time ago that if the second assumption is violated, the relaxation will be slower than expected from the tube theory. Thus, the validity of both Rouse and tube theories clearly depends on the coupling and cross-correlations between orientation relaxation of di erent chains in the melt.

Various experiments suggested that there is a speci c interaction in polymer melts called nematic interaction, which orient the surrounding polymer segments toward the same direction. Doi *et al.*[33][34] introduced models which account for the nematic interaction for reptation and Rouse dynamics. In monodisperse melts, they found that the stress-optical law was valid in this model, and the stress-optical coe cient became larger with increasing strength of the nematic eld. The theory was also generalized for binary blends, which showed that the relaxation of the short chains were not independent of the long chains relaxation due to the nematic interaction.

Experimentally, orientation coupling was investigated by a combination of di-electric dichroism and birefringence by Ylitalo *et al.*[31], and by NMR by Graf *et al.*[35]. In the rst group of experiments, one of the components in binary mix-ture was labeled and its orientation relaxation was measured after a step-strain experiment. The labeling was achieved by replacing a portion of hydrogens on the polymer backbone with deuterium and then performing the measurements at the infra-red wavelength of the carbon-deuterium vibrational absorption. It was shown that the short component orientation is not fully relaxed until the longest relaxation time of the long component, and that the relaxation of short component

coe cient " 0:18 was found. They argued that the di erence can be explained

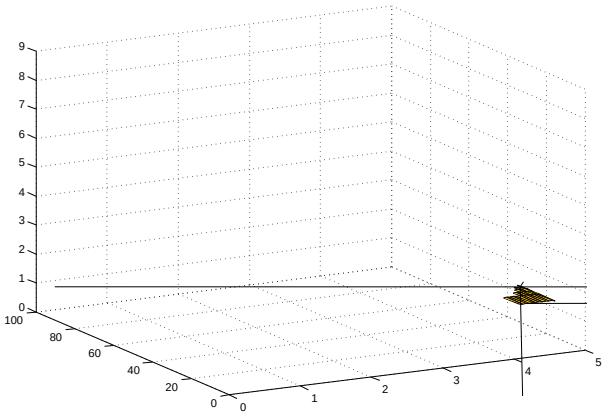

Figure 2.29: $g(r;\ )$ of the system with $=0{:}6\quad ^{3}$.

Figure 2.30: $g(r;\ )$ of the system with $=0{:}85\quad ^{3}$.

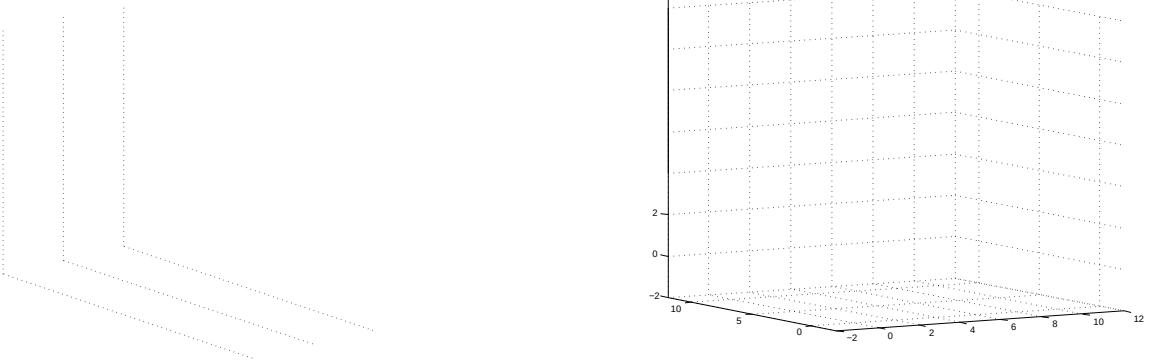

Figure 2.31: $g(r;\ )$ of the system with $=1{:}15\quad ^{3}$.

Figure 2.32: Bonds positions in the simulation box of the system with $= 1{:}15\quad ^{3}$.

$g(r;\ )$ was calculated in the systems with di erent densities(Fig.2.29 and Fig.2.30) and $g(r) = \int_0^{R=2} g(r;\ )d$. From these two gures, we can see the following general features:

would be trapped by the surrounding dumbbells and feel di cult to jump out the \cage". The coupling e ect between two dumbbells at short distance becomes larger with increasing density. The system crystallized if we increase density to 1:15 ^{3} (Fig.2.32), with dominant orientation being = 60^{o}, which due to the spheres are close packed. Now we turn our attention to the same e ect in polymer chains.

2.6.2 Short-range orientational coupling

Orientational cooperativity in polymer melts can arise due to short-range forces acting on the segmental level. It was discussed by Doi *et al.*[33] that the strength of this interaction can be measured by using the bulk and shorter component relaxations after short chain's relaxation time(Eq.2.22).

In our notations, this coupling parameter " can be expressed as following:

$$"(t) = \frac{E_s(t)}{S_{tot}(t)} \frac{S_{tot}(0)}{E_s(0)} = \frac{E_s(t)}{S_{tot}(t)} = \frac{A_s(t) + C_{ss}(t)\ '_s + C_{sl}(t)\ '_l}{S_{tot}(t)} \qquad (2.25)$$

It is shown in Fig.2.33 and Fig.2.34 for di erent composition of the binary blends of exible and semi- exible systems. In exible systems, short and long components have chain lengths N_1=10 and N_2=100 respectively and all " equal to 0:28 after short component relaxed. However, this coupling parameters are di erent in the particular semi- exible systems with N_1= 5; N_2=100 in Fig.2.34. The range of " is from 0:28 to 0:35 depending on the concentration of the short component, which is caused by the dynamics of the chain ends. If we use longer short chains(N_1=30), " are the same at di erent compositions(0:35). The results from our simulations are consistent with Baljon's results[36].

However, Eq.2.25 does not include the cross-correlation function between the long chains $C_{ll}(t)$, which is an important contribution to the relaxation function at longer times. This exclusion indicates that " is not an appropriate parameter to present coupling e ect at longer times. And this coupling parameter can only be measured after short chains

Figure 2.33: Coupling parameter $''$ in binary blends of flexible chains.

Figure 2.34: Coupling parameter $''$ in binary blends of semi-flexible chains.

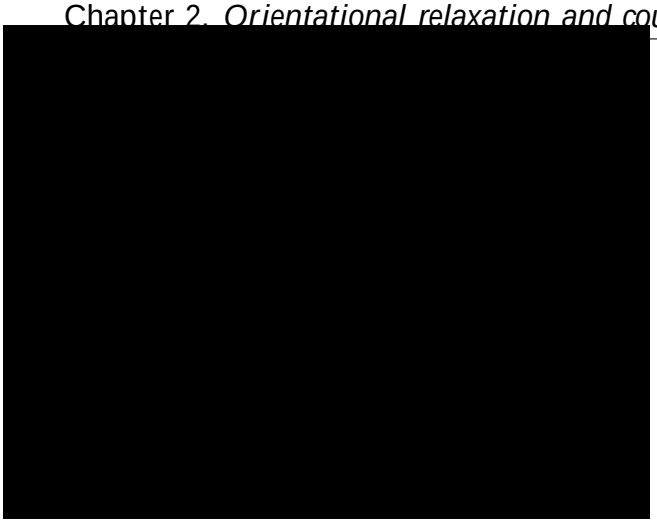

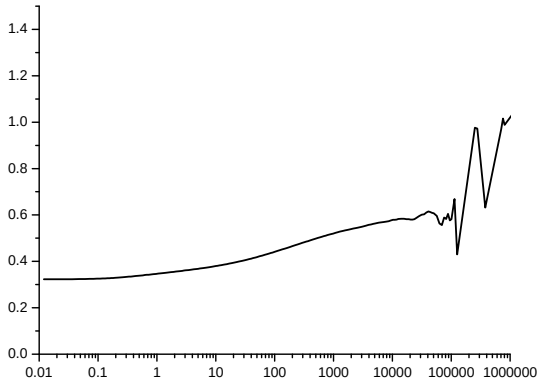

Figure 2.44: Coupling parameter (t) of soft potential in monodisperse melts of semi- exible chains.

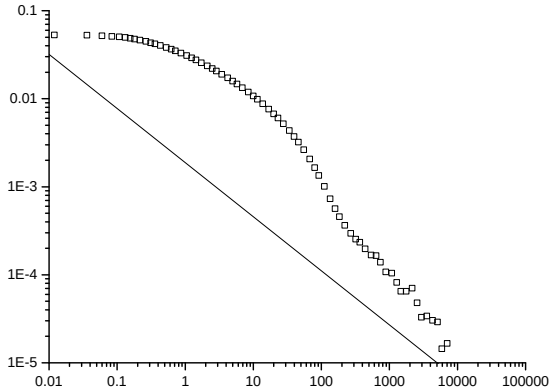

Figure 2.45: Prediction from Eq.(2.30)(lines) and the measured total relaxation(symbols) of binary blend of exible systems.

must be modi ed accordingly.

2.6.6 Universality of our coupling parameter

The universality of time-dependent coupling parameter (t) has non-trivial consequences for polymer blends. Indeed, a requirement that (t) is the same in monodisperse melts and in their blends can be written as

$$\begin{aligned} 1 \quad (t) = \frac{A_s(t)\,'_s + A_l(t)\,'_l}{S_{tot}(t)} &= \frac{A_s^{mono}(t)}{S_s^{mono}(t)} = \frac{A_l^{mono}(t)}{S_l^{mono}(t)} \\ ) \quad \frac{A_s(t)\,'_s + A_l(t)\,'_l}{S_{tot}(t)} &= \frac{'_s A_s^{mono}(t) + '_l A_l^{mono}(t)}{'_s S_s^{mono}(t) + '_l S_l^{mono}(t)} \end{aligned} \qquad (2.29)$$

It immediately follows from here that if the auto-correlation functions are the same in the mixtures as in the monodisperse systems ($A_s(t) = A_s^{mono}(t)$ which is true for unentangled systems), the simple mixing rule for the total orientation relaxation

$$S_{tot}(t) = '_s S_s^{mono}(t) + '_l S_l^{mono}(t) \qquad (2.30)$$

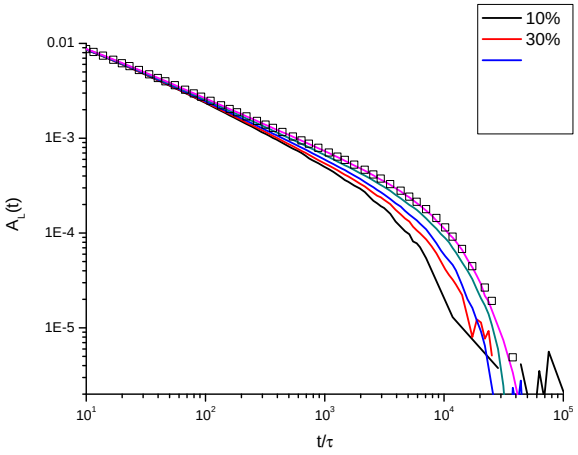
10%
30%
0.01
1E-3
1E-4
1E-5
$A_L(t)$
10^1
10^2
10^3
10^4
10^5
t/τ

Chapter 2.

Figure 2.48: (t) of exible and semi- exible chains.

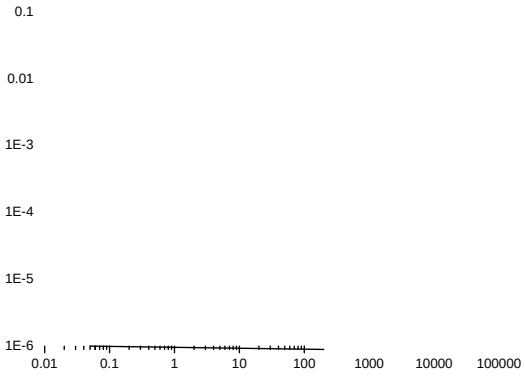

Figure 2.49: Total relaxation functions(symbols) and the prediction(lines) of exible chains from Eq.2.38.

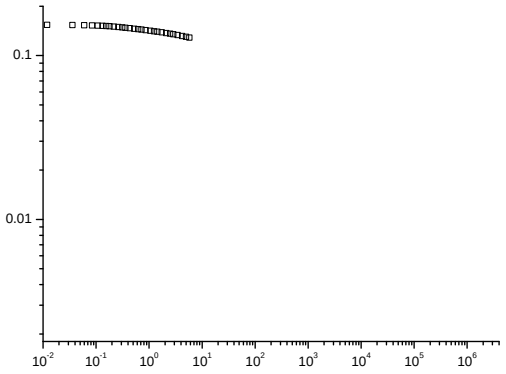

Figure 2.50: Total relaxation functions(symbols) and the prediction(lines) of semi- exible chains from Eq.2.38.

equations provide a simple relation of our coupling parameter with the Doi's parameter:

$$
\begin{aligned}
''(t) &= \frac{E_s(t)}{S_{tot}(t)} \\
&= \frac{S_s^{mono}(t) + \frac{(t)}{2}\,'_l[S_l^{mono}(t) \quad S_s^{mono}(t)]}{'_s S_s^{mono}(t) + '_l S_l^{mono}(t)} \\
&\quad \frac{1}{2} \quad (t) \qquad (t > \ _s): \qquad (2.37)
\end{aligned}
$$

Chapter 2.

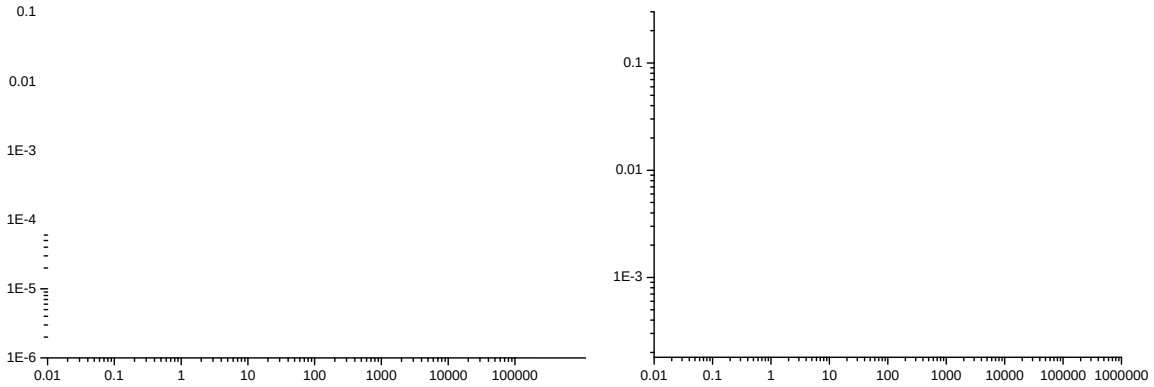

Figure 2.51: Total relaxation functions(symbols) and the prediction(lines) of exible chains from Eq.2.39.

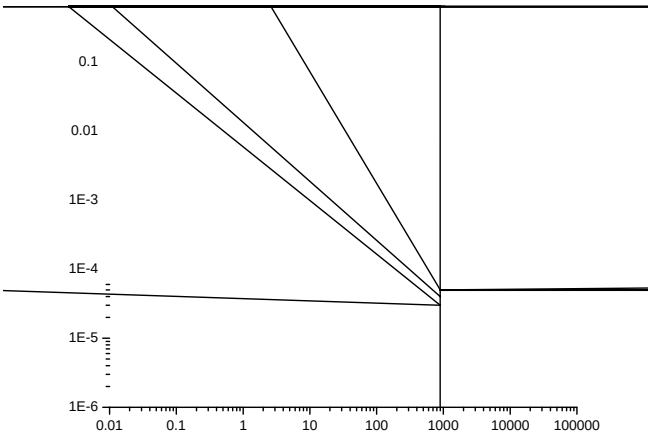

Figure 2.53: Total relaxation functions(symbols) and the prediction(lines) of exible chains.

Figure 2.54: Total relaxation functions(symbols) and the prediction(lines) of semi- exible chains.

However, if the long and short chains have widely separated molecular weights M_s and M_l, the slow relaxation behaviour of the long chain in the blend is similar to that in a solution having the same volume fraction $'_l$ of these chains[38]. The molecular weight of solvent is well below the entanglement molecular weight and the relaxation of the long chain in the solution is only a ected by their mutual entanglements. In the binary blends, the short chains are in a slightly entangled state, and the relaxation of the long chains is a ected by the entanglements with the short chains. According to constraint release mechanism, the relaxation of the long chains is dominated by the CR mechanism if the Struglinski-Graessley parameter $r_{SG} = M_l M_e^2 / M_s^3$ is larger than a threshold value of about 0:5. In our simulations of entangled binary blends, the SG parameters is 1:25 for semi- exible chains, which is larger than the threshold value.

Now we are going to check whether the length of the short chain a ects the relaxation of the long chain or not in the exible systems. $N = 100$ is chosen for the long chains as in previous runs, and the dumbbells are chosen for representing the solvent. Auto-correlation function $A_l(t)$ of long chains are in good agreement in these two systems(Fig.2.55). Now we can use the auto-correlation function of long chain in the solvent to predict the total relaxation function of binary blends. The predictions and the target relaxation functions are both shown in Fig.2.56.

Thus a qualitative agreement between the solutions and the blends suggest that in this case the short chains in the blends behave as a solvent in the terminal

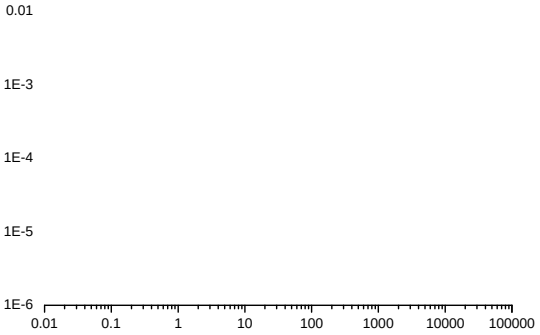

Figure 2.55: Auto-correlation function $A_l(t)$ of long chains in binary blends(symbols) and solutions(lines).

Figure 2.56: Total relaxation functions(symbols) and the prediction(lines) of exible chains.

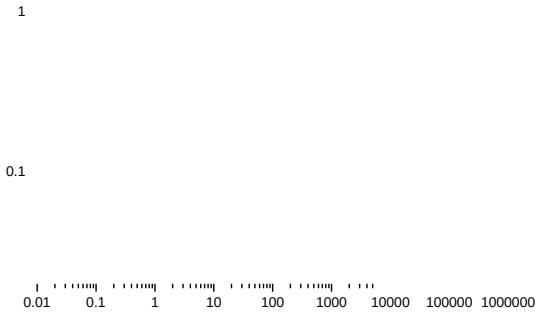

Figure 2.57: Coupling parameter (t) of exible chains at di erent coarse-graining level. The starting point

Chapter 2.

Chapter 2.

Chapter 3

Microscopic simulations of melts in start-up shear

3.1 Overview

In real world, a rheological measurement tells one how \hard" or \soft" the material is, which depends on the time scale at which the material is probed. A rheometer is normally used to measure rheological properties of a complex uid as a function of rate or frequency of deformation. There are two widely used methods to obtain rheological property of the complex uid. One is applying a shear ow on the material and measuring the resulting stress, the other is applying a shear stress and measuring the resulting shear strain. As mentioned before, the shear stress

fracture[42] and shear banding[43][44]. As a result, very few experimental data have been published that can be used by the theoreticians.

The Doi-Edwards tube theory[1

is the dominant contribution to the constraint release. Chain stretching describes a mechanism that the length of the occupied tube exceeds its equilibrium value. In the Doi-Edwards model the orientation of the chain relaxes at the reptation time $_d$ while the chain stretch occurs at a rate determined by the Rouse time $_R$. These two time scales are well separated in entangled systems. The e ect of chain stretch becomes signi cant when $\dot{}_R$ 1. The Doi-Edwards-Marrucci-Grizzuti(DEMG) theory[47][48][49] adds stretch to the basic DE model. The new theory improves the transient predictions in start-up of shear. The DEMG model predicts that the transient overshoots in shear stress and normal stress grow in size with shear rate and the strain at maximal stress at overshoots grows with shear rate, which were observed experimentally. However, The DEMG theory is less successful in steady state of shear. It still predicts a maximum of shear stress.

In this chapter, steady shear is applied to our molecular dynamics simulations and the properties of the material in both transient and steady states are investigated. Surprisingly, we observe a shear stress maximum at steady state around $\dot{}$ 1= $_d$ in a su ciently long chain system, which indicates that a shear banding

is an acceptable method if one is interested in nano-con ned ows, where the spacial inhomogeneity is important in the simulations. However, if one is concerned with bulk properties far away from the surface, the explicit use of the boundary is inappropriate. An alternative to using \solid" wall boundaries is to drive a ow via a suitable implementation of periodic boundary conditions. The most useful method is using Lees-Edwards boundary conditions[50] for planar shear ow. The original simulation box is replicated in all directions by periodic images. Monomers interact via their pair-potential forces under Newton's second law. The di erence between the periodic boundary condition in equilibrium simulations and the one in non-equilibrium simulations is that the periodic image boxes in di erent layers have strain di erence $N_L L_y \dot{} t$ in shear direction, where N_L is the number di erence of the layers, L_y is the length of the simulation box in y-direction, $\dot{}$ is the shear rate and t is the shear time.

However, this boundary condition has a serious disadvantage that it takes time for the e ects of translation of atoms between boundaries to communicate throughout the uid, which means a linear velocity pro le will not be imposed immediately, but will evolve only after a su ciently long time. The rst homogeneous NEMD algorithms was proposed by Hoover *et al.*[51] which was based on

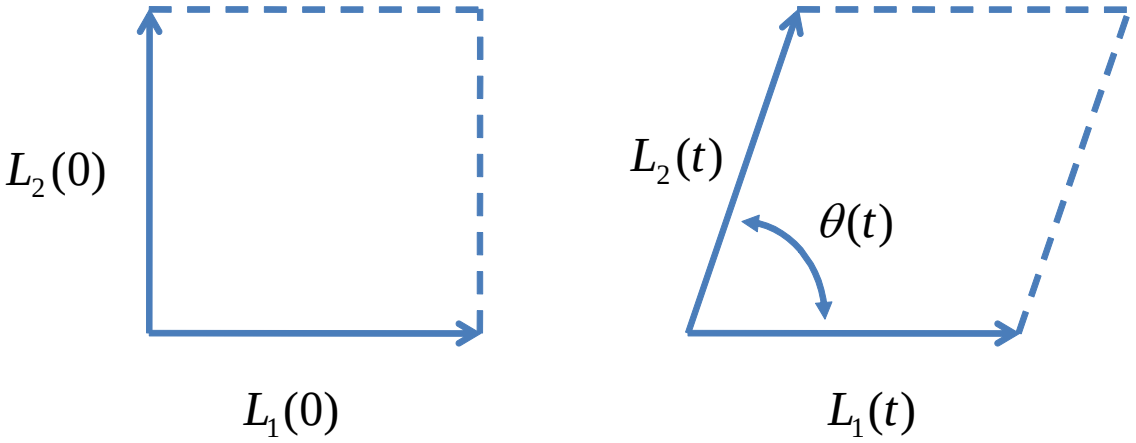

Figure 3.1: 2-dimensional representation of simulation box vectors. As $t \to 1$, $(t) \to 0$ and $jL_2j \to 1$, whereas jL_1j remains the same.

Now we will discuss the implementation of the suitable periodic boundary condition that are compatible with the SLLOD equations of motion for planar Couette ows in which the fuild ows in the x-direction with a velocity gradient $\dot{\gamma}$ in the y-direction. As boundaries must be compatible with the imposed streaming velocity pro le, we rst calculate the strain rate tensor:

$$\nabla v = \begin{pmatrix} \frac{\partial v_x}{\partial x} & \frac{\partial v_y}{\partial x} & \frac{\partial v_z}{\partial x} \\ \frac{\partial v_x}{\partial y} & \frac{\partial v_y}{\partial y} & \frac{\partial v_z}{\partial y} \\ \frac{\partial v_x}{\partial z} & \frac{\partial v_y}{\partial z} & \frac{\partial v_z}{\partial z} \end{pmatrix} = \begin{pmatrix} 0 & 0 & 0 \\ \dot{\gamma} & 0 & 0 \\ 0 & 0 & 0 \end{pmatrix} \tag{3.7}$$

The evolution of the boundaries is applied by the same equation of motion.

Figure 3.2: Lagrangian-Rhomboid and Sliding-Brick periodic boundary conditions.

which creates a problem. If $t \to \infty$, then $\dot{\gamma}(t) \to 0$ and $|L_2| \to \infty$, which is not practical. Two equivalent algorithms were introduced to fix this situation. The first of these is to deform the simulation box until it reaches a preset angle θ_p, at which time the box is changed back to the original cubic shape. In this method, the transformations do not happen very frequently and box sides lengths do not get too large. The second method is to use Lees-Edwards \sliding-brick" periodic

3.2.2.3 Nose-Hoover thermostat

At each time-step, the velocities of all particles are rescaled by an additional dynamic variable

$$\underline{r}(t + \ t) = \underline{r}(t) + \frac{f(t)}{m} \ t \tag{3.12}$$

$$\text{-} = C(T \quad T_C) \tag{3.13}$$

where C is a constant parameter that can be set for optimal results. This method modi es the velocities \gently".

3.2.2.4 Berendsen thermostat

Comparing to the constraint method, Berendsen thermostat is trying to correct the deviations of the actual temperature T_C from the prescribed one T by multiplying

uctuation-dissipation theorem, the relations

$$^2 = 2k_B T \tag{3.21}$$

and

$$w^R(jrj) = \sqrt{w^D(jrj)} \tag{3.22}$$

must hold[57]. The usual choice is

$$w^R(r) = \sqrt{w^D(r)} = \begin{cases} 1 & r=r_c;\quad r < r_c \\ 0; & r \quad r_c \end{cases} \tag{3.23}$$

Another choice, which is computationally more e cient, is

$$w^R(r) = w^D(r) = \begin{cases} 1; & r < r_c \\ 0; & r \quad r_c \end{cases} \tag{3.24}$$

We use Eq.(3.23) in most of our simulations except when a large shear rate $\dot{} > 0{:}1 \quad ^1$ was applied on the

Figure 3.3: Velocity pro le of different chain lengths. *np* is the number of the particles in the system.

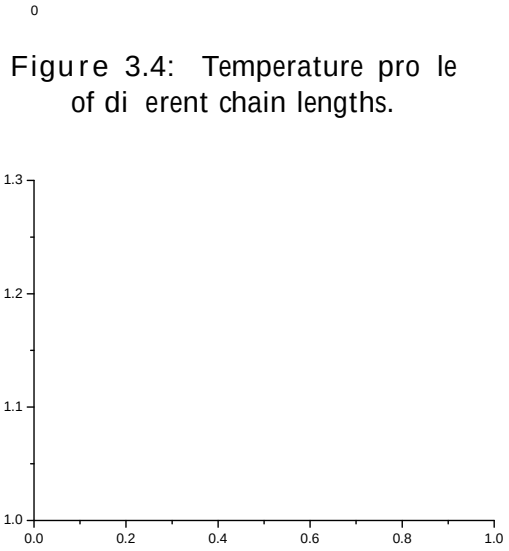

Figure 3.4: Temperature pro le of di erent chain lengths.

Figure 3.5: Velocity pro le of different number of chains.

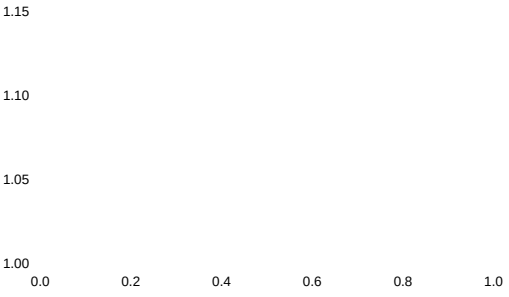

Figure 3.6: Temperature pro le of di erent number of chains.

Figure 3.7: Velocity pro le of different shear rate.

Figure 3.8: Temperature pro le of di erent shear rate.

length is, the slower the particle is than it should be, which means the friction term is overestimated. The temperature pro les are shown in Fig.3.4. The temperature near the boundaries is higher than the one in the center, which can be explained by the shear heating as the momentum exchanged around the boundaries.

We also run simulations with the same chain lengths and shear rates but with

results as in the previous case (square symbol in Fig.3.11 and 3.12). Constraint thermostat method is used to keep the temperature to the desired one (star symbols in Figs.3.11 and 3.12). All the results discussed later are obtained from this combination of Langevin, SLLOD and constraint thermostat method.

As we know, polymer chains will be stretched and oriented under shear, the size of the long chains will be larger than the length of the simulation box and the chains will interact with themselves through the periodic boundaries. In order to eliminate this defect, we need to use non-cubic simulation box. Suppose the shear direction is along the x-axis, the direction of velocity gradient is along the y-axis. The first method we used is putting all chains into a reshaped box which has the length ratio on $x;y;z$ equal to $2:1:1$. The simulations run for a long time around several terminal relaxation time $_d$ of the longest component to make sure the system is in equilibrium, and then we start to shear the material. The second method we used is that the configuration of the chains is obtained from the previous simulations in equilibrium which has a cubic simulation box. Another copy of this configuration is made. And we put this copy next to the original one along the x $_d$

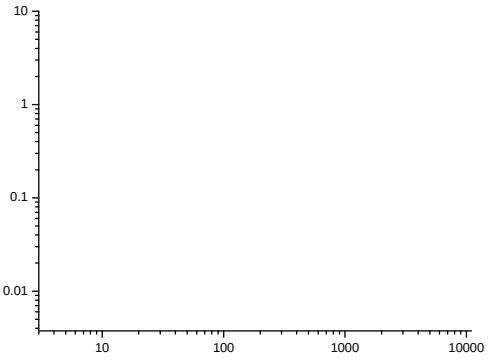

Figure 3.13: $_{xy}$ and two normal stress in di erent simulation boxes.

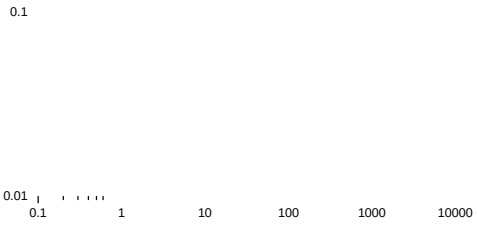

Figure 3.14: $_{xy}$ in one single run and averaged over ten jobs.

3.2.4 Averaging methods

As we know the number of particles involved in the MD simulations is ranging from several hundred to several hundred thousand, which is a small number comparing to the number of molecules used in experiments. So a careful averaging method is essential in the simulations. Logarithmic bins in time are introduced. Suppose a quantity $C(t)$ of the system is measured at time t since the start of shear. A series of averaging time internals $t_i^0; i \ 2 \ \mathbb{Z}^+$ where $\mathbb{Z}^+$ is the set of non-negative integer numbers, is introduced as following:

$$t_0^0 = D \tag{3.25}$$

$$t_i^0 = D \ M^i \tag{3.26}$$

where D is a constant standing for the rst time interval, and M is a multiplication factor. In our simulations, D and M are set to $8dt$ and 1:1 respectively, where dt is the simulation time step. Suppose the shear starts from t_0, $t_i = t_0 + \sum_{k=0}^{i-1} t_k^0$, then

$$C(t_i + \frac{t_i^0}{2}) = \frac{1}{t_i^0} \int_{t_i}^{t_i + t_i'} C(t)dt \tag{3.27}$$

With this algorithm we obtain around 25 data points in each decade of time(black symbols in Fig.3.14). As the system size is quite small(9000 particles), the signal is not very good in just one single run. We run 10 simulations with the same parameters except the seed of random force generator, and then average over all these data(red symbols in Fig.3.14). The curve is much smoother and more reliable

than the data from the single run. However, the signal is still noisy at short times as the averaging intervals t_i^0 at short times are much smaller comparing to the ones at longer times. Note however that the early time behaviour can be obtained from the $G(t)$ data as demonstrated later, so these data are not essential.

3.3 Monodisperse melts under shear

0.1 1 10 100

Figure 3.21: Shear-stress maximum as a function of $\dot{\gamma}N^2$.

Figure 3.22: Strain at shear-stress maximum as a function of $\dot{\gamma}N^2$.

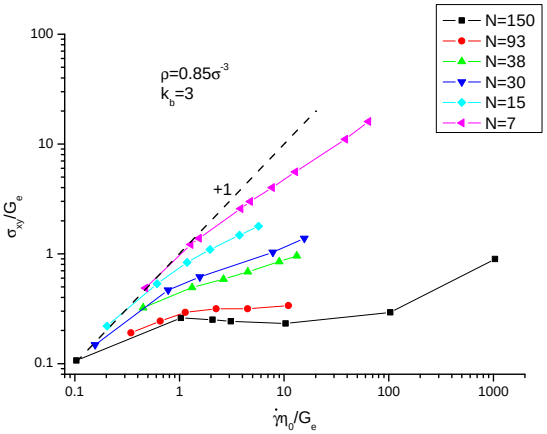

Figure 3.23: Shear stress *xncfunction of* $\dot{\gamma}^2$:

Fig.3.23-Fig.3.26. The first and second normal stresses increase as the shear rate increases in all systems. Surprisingly if the first and second normal stresses are plotted as a function of $\dot{\gamma}N^2$, all curves pass through a particular point. The ratio of the second and the first normal stresses is about 1=7 at small molecular weight, which is in good agreement with the Doi-Edwards theory and the experimental results from Schweizer *et al.*[59][42]. With increasing the chain length, a negative

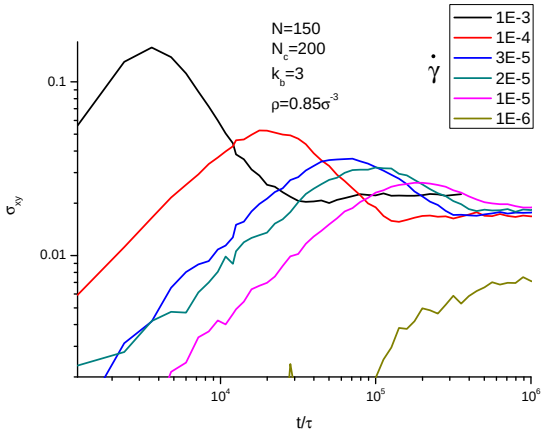

Figure 3.27: $_{xy}(t)$ of semi- exible chain with $N = 150$ at dif- ferent shear rates _.

Figure 3.28: Cox-Merz rule in our simulations. Solid symbols are stress at steady state. lines are complex viscosity times shear rate _.

that the Cox-Merz rule works for the short chain systems, but not for the longer chains.

3.3.3 Stress-optical law in monodisperse melts

Before doing other analysis, let us check if the stress optical law works in our shear simulations. Chain lengths $N = 30; 150$ are chosen for the monodisperse melt. First, the stress and orientation relaxation functions in the equilibrium state are shown in Fig.3.29. The stress-optical law works for the time scale larger than 500 . Now we would like to see whether the stress-optical law works in the shear situation. The stress and the orientation of the systems divided by the shear rates are shown in Fig.3.30. In the transient state, both stress and orientation collapse onto their respective master curves. The power law exponent of stress is around 0:5. However, the power law exponent of orientation is around 0:8. It looks like the stress-optical rule does not work at short times. As we know, the viscosity in shear can be expressed by the integral of the stress relaxation function $G(t)$ in equilibrium(Eq.3.28). The orientation in shear can also be expressed by the integral of the orientation relaxation function in equilibrium. As shown in Fig.3.29 stress and orientation behave di erently at short times. There are oscillations in the stress relaxation function due to bond uctuations, and it is almost constant

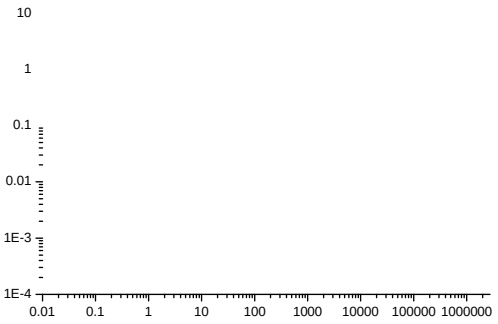

Figure 3.29: Stress and orientation relaxation functions in the equilibrium where called stress-optical coe cient is 1:28.

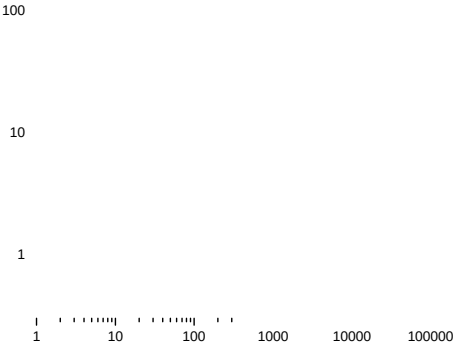

Figure 3.30: Stress $_{xy}$(lines) and orientation S_{xy}(symbols) as a function of time at di erent shear rates, where = 1:28 is the stress-optical coe cient from the equilibrium simulation.

Figure 3.31: Instantaneous position(a) and mean path(b) of a polymer chain with chain length equal to 150 and bending energy equal to 3.

Figure 3.32: Orientation from instantaneous positions is compared to the one obtained from mean path.

for orientation relaxation function, which explains why the slope of orientation in shear is closer to 1. After the overshoot, the stress and the orientation are in qualitative agreement(Fig.3.30). In conclusion, the stress-optical law works quite well at small shear rates _ < 1=500 and at long time $t > 500$.

3.3.4 Orientation from mean path

We introduce a notion of the *mean path* which is a collection of the bead coordinates r_i averaged over the time interval $_{av}$

$$\hat{r}_i(t) = \frac{1}{_{av}} \int_{t\ _{av}}^{t} r_i(t')dt' \tag{3.31}$$

Both instantaneous con guration and the mean path of a polymer chain with chain length N=150 are shown in Fig.3.31. These con gurations show that the mean paths are smoother than the chains and the short time fast uctuations are suppressed by the averaging procedure. The averaging time interval should be chosen with care. In Fig.3.31, the averaging time was chosen to be $_{av}$=1200 . Now we would like to check whether the mean path will keep the property of the orientation of the original chains or not. The orientation obtained from the instantaneous positions and the mean paths are both shown in Fig.3.32. The monodisperse melt with chain length N=93 and bending energy k_b=3 was chosen. The result from the mean paths is in good agreement with the one from the instantaneous positions, so we can claim that mean paths contains all information about the orientation of the polymer chains. In the future, we will analyse our system by using mean path instead of instantaneous positions, which can erase faster uctuation e ects. We note that orient function $S(t)$ obtained from instantaneous positions stored every 1200 is much noisier than the one shown in Fig.3.32.

3.3.5 Con guration of polymer chain in transient state and steady state

DNA tumbling has previously been observed in dilute unentangled solutions[60] and in entangled solutions[61]. We would like to investigate the tumbling in polymer melts for the rst time in our simulations.

In Fig.3.33, we can see the evolution of the single chain conformation in a monodisperse melt. The sample has the chain length N=93 with bending energy

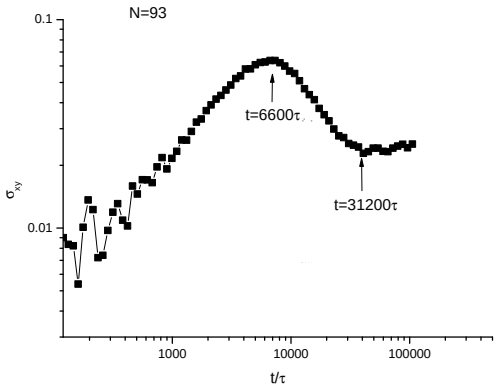

Figure 3.33: Con guration of the polymer chain at di erent state during shear.

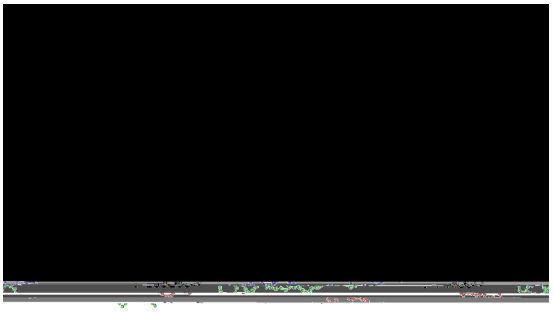

Figure 3.34: The corresponding conformation of the chain during tumbling in steady state at shear rate _ = 0:00032 [1].

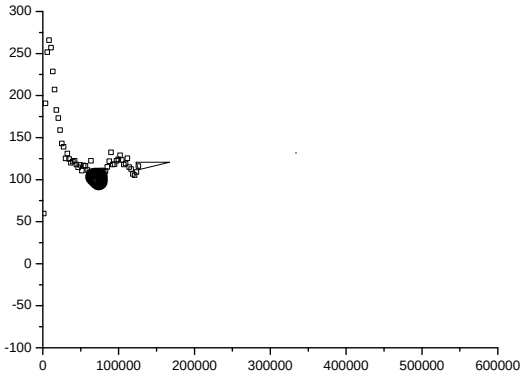

Figure 3.35: End-to-end vector R_e of one chain and orientation of the system in shear.

$k_b = 3$ and density $= 0{:}85$ [3]. Before the shear starts($t = 0$), the chain is a random walk in 3D-space. After shearing starts, the chain is stretched in shear direction(x-axis).

Beyond the stress overshoot, we observed that the chain also spends a small fraction of the time to tumble as shown in Fig.3.34. In Fig.3.35, we show each component of the end-to-end vector R_e of the chain which was plotted in Fig.3.34. The black symbols are the orientation of the system. y and z components of R_e are not strongly a ected by the shear. They both uctuate around the average

Chapter 3.

Figure 3.36: G', G'' of PI-30k(symbols) in experiment and N=93 with k_b=3(lines) in the simulation.

30k(symbols) in experiments and N = 93 with k_b = 3(lines) in the simulation.

G' and G'' at low frequencies,

$$1s \quad) \quad 8300 \tag{3.33}$$

$$1Pa \quad) \quad 1{:}48 \quad 10^{\ 7}\,''=\ ^{3} \tag{3.34}$$

where , '' and are the units of time, energy and length in the simulations.

The mapping coe cient between PI molecular weight in the experiment and number of beads of semi- exible chains in the simulations is

$$\frac{M_e^{exp}}{N_e} = 0{:}36 kg/mol \tag{3.35}$$

All the parameters of the simulations will be calculated from these three mapping coe cients.

Thehr-424Tfviscosiwy-4243fromerulationsw

pigu-igu.-3248The Wterumbors usd n PIPnd PI-Psamples-320(Pne)]TJ/F35 11.955

Figure 3.38: Comparing PI-2k shear experiments(symbols) with $N = 7$ simulation results(lines) according to the same Weissenberg number.

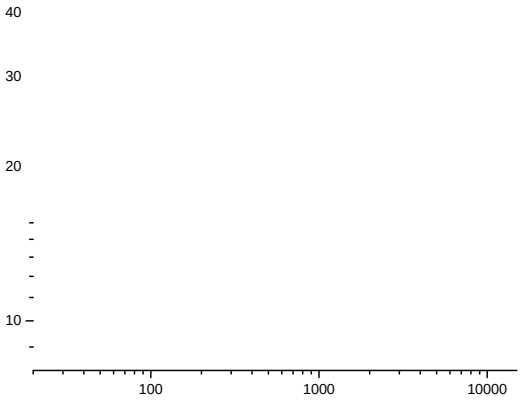

Figure 3.39: Comparing PI-4k shear experiments(symbols) with $N = 15$ simulation results(lines) according to the same Weissenberg number.

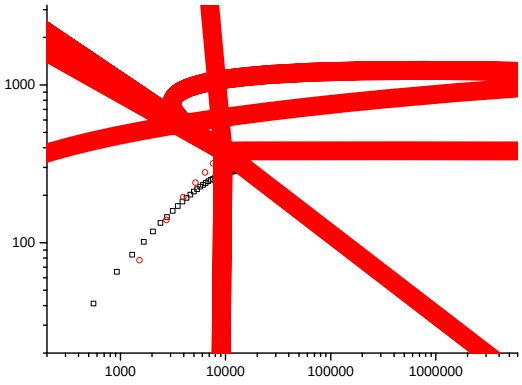

Figure 3.40: Comparing PI-14k shear experiments(symbols) with $N = 38$ simulation results(lines) according to the same Weissenberg number.

Figure 3.41: Comparing PI-30k shear experiments(symbols) with $N = 93$ simulation results(lines) according to the same Weissenberg number.

simulations is in qualitative agreement with the viscosity from the experiments. We suppose the reason for some disagreement is that the local structures of PI and the semi- exible Kremer-Grest model are di erent from each other. The semi- exible KG model is more sti than polyisoprene. We believe the results from exible systems can be in better agreement with experiments which is a subject of future study. Another reason might be inaccurate mapping parameters. We note that for every new set of parameters new simulations must be performed, which makes it a very expensive procedure.

experiments was obtained. We suppose the quantitative disagreement is due to di erent sti ness of PI sample and semi- exible KG model. In order to obtain a quantitative agreement with the experiments, we will study the simulations of more exible chains and improve our mapping procedures.

Chapter 4

Coarse-grained simulation of polymer melts

4.1 Overview

As we explained in chapter 1, the molecular dynamics(MD) simulations are not suited to the study of phenomena which occur on time and length scales that are

is the gradient of the free energy of the con guration of the mesoscopic \blobs". Second is the dissipative force which indicates that the motion of the mesoscopic \blobs" is retarded by friction. The last is the thermal force due to the continual collision e ect on the mesoscopic \blobs". The dissipative and thermal forces must be related to each other to ensure that both forces do not alter the equilibrium ensemble distribution, which is stated by the uctuation-dissipation theorem.

As far as static properties are concerned, the determination of e ective in-

distribution function of the microscopic system. They introduced tting parameters , and minimized a eld with respect to .

On the other hand, we need information about the dissipative and thermal forces for the dynamic properties. Normally the dissipative force is taken as a linear function of momenta for the microscopic particles. However, the friction coe cient of mesoscopic particles also depends on the con guration of particles, and it is important to account for both time and spatial dependency. Akkermans and Briels[69] coarse-grained one polymer chain in a melt to a single dimer of mesoscopic particles, called blobs. By using the projection operator formalism they separated the total force on the chain into the thermodynamic mean force, dissipative force and uctuation force, and derived the equations of motion for the dimer. Dimer properties of the microscopic and the coarse-grained model were shown to be in reasonable agreement.

In this chapter, we only concentrate on the static properties of the polymer chains, so we make the dissipative and thermal forces of mesoscopic \blobs" independent of time and space. The whole chain was coarse-grained into a single \blob", and we aim to study the interaction forces between the blobs rather than

two molecules.

Suppose monomers $i; j$ are two monomers which belong to two di erent molecules $a; b$ respectively. f_{ij} is the force between monomers i and j. $R_a; R_b$ are the coordinates of the center-of-mass of chains a and b. We then de ne a projection force f_{ab} between blobs a and b as

$$f_{ab}(jD_{ab}j) = \sum_{i;j} \frac{f_{ij} \quad D_{ab}}{jD_{ab}j^2} D_{ab}; \quad 8i \ 2 \ a; 8j \ 2 \ b \tag{4.1}$$

$$D_{ab} = R_a \quad R_b \tag{4.2}$$

where D_{ab} is the distance vector between blobs a and b. f_{ab} and D_{ab} have the same direction.

In this de nition, we do not include the case when two monomers are in the same blob, which means the forces inside the blobs are not considered for this projection procedure. If we divide the molecules into several subchains and coarse-grain the monomers in one subchain into a blob, the projection force between these blobs of subchains will be very di erent from non-bonded one due to connectivity. In this work, we will study the projection force between non-bonded blobs rst. Bonded blobs are left for the future study. Before using the projection procedure in Kremer-Grest microscopic simulation, we should assess if this method is reasonable or not. A Rouse chain is replaced by a blob between two walls and the distribution function of the center-of-mass of the Rouse chain between the walls in microscopic simulation is compared to the one from the coarse-grained simulation.

4.3 Rouse model between two walls

In the Rouse model, the excluded volume interaction and the hydrodynamic interaction are disregarded and the interaction potential is written as:

$$U(fR_ig) = \frac{3k_BT}{2b^2} \sum_{i=0}^{N-1} (R_{i+1} \quad R_i)^2 \tag{4.3}$$

Figure 4.1: The center-of-mass distribution function of the Rouse chain between two walls in microscopic(red line) and coarse-grained(open symbols) simulation.

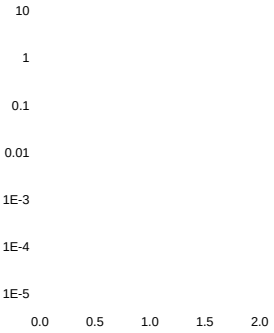

Figure 4.2: Projection force function $f(r)$ of Rouse chain from solid wall in log-linear(left) and linear-linear(right) plots. The line is the best fit data which has the expres-

0 2

Figure 4.3: The center-of-mass distribution function of a Kremer-Grest chain between two walls from microscopic simulation(red line) and from coarse-grained simulation(open symbols).

Figure 4.4: Magnitude of the projection force function $f(r)$ of Kremer-Grest chain from solid wall in log-linear plots. The line is the best t data which has the expression as Eq.(4.8).

4.3.2 Coarse-grained simulation

Now we can use this best t projection force $f_{fit}(x)$ in the coarse-grained simulation. A single particle is placed between the two walls. The potential from the wall was changed from Lennard-Jones potential to

$$U(x) = \int_0^x f_{fit}(x')dx': \tag{4.7}$$

The obtained distribution function(open squares in Fig.4.1) is in excellent agreement with the one obtained from the original microscopic simulation. However, a Rouse chain is a random walk in space and there is no long range interaction between the beads which have large chemical distance. In next section we would like to ask whether this projection procedure is also valid for the Kremer-Grest model.

4.4 Single Kremer-Grest chain between two walls

Similar to the previous section, we place one Kremer-Grest chain with length N=10 instead of a Rouse chain between two walls separated by a distance of 16 . The chain is not Gaussian in vacuum due to excluded volume e ects, and the size

of the chain is larger than $\sqrt{Nb^2}$. As the beads repel each other and the bonds can not cross each other, the dynamics of Kremer-Grest model are different from the Rouse chain.

The distribution function was measured and is shown by red line in Fig.4.3. The force on the KG chain from the walls(symbols in Fig.4.4) was also measured by using projection force method. The best fit is shown by red line in Fig.4.4, where the numerical expressions are

$$f_{fit}(x) = \begin{cases} \exp(-3.2473x + 7.3307); & 0 < x \leq 1.9 \\ \exp(-2.0149x + 5.0317); & 1.9 < x \leq 4.05 \\ \exp(-7.0604x + 25.329); & 4.05 < x \leq 5.0 \\ 0; & x > 5.0 \end{cases} \tag{4.8}$$

Then we applied this best fit projection force $f_{fit}(x)$ to the coarse-grained simulation. The obtained distribution function(open squares in Fig.4.3) is in excellent agreement with the one from the original microscopic simulation.

From the previous two sections, we conclude that the local structure of the polymer chain does not affect the validity of this procedure, which indicates that the force projection method might be useful for reducing the number of degrees-of-freedom of the system.

4.5 Kremer-Grest model in vacuum

In the previous sections, we were using the force projection method to measure the force on the chain from the walls. Now we would like to study this method for pairs of Kremer-Grest chains in vacuum. The pure repulsive Lennard-Jones potential is chosen for the simulations.

Normally, the mean square internal distance function and the radius of gyration are the two common objective functions which describe the structure of the chains. The mean square internal distance function $\langle R^2(n)\rangle/n$ of chain length $N = 100$

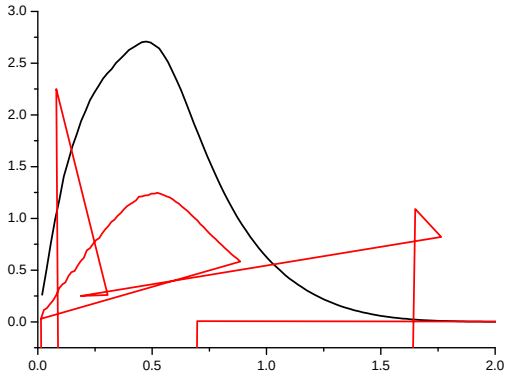

Figure 4.7: Vacuum projection

Chapter 4.

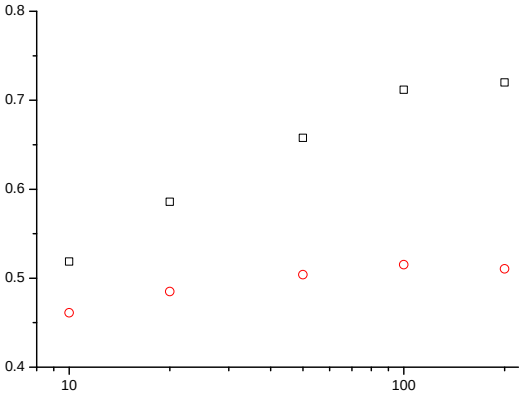

Figure 4.18: Radius gyration as a function of chain lengths.

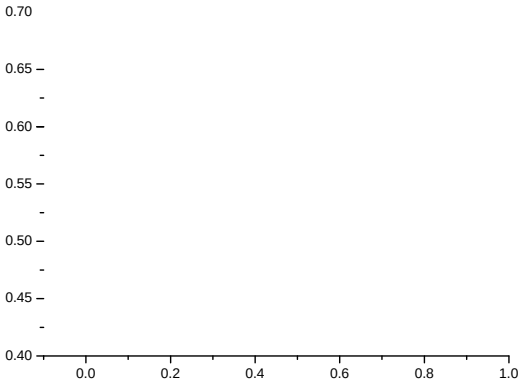

Figure 4.19: Radius gyration as a function of density of the system.

of di erent chain lengths are shown in Fig.4.18. $R_g(N) = \sqrt{N}$ increases with increas-

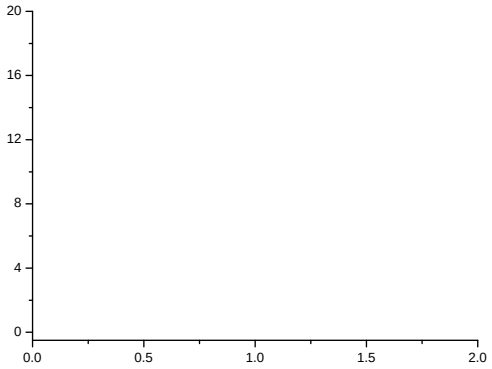

Figure 4.20: Projection force of $N=10$ at di erent densities.

Figure 4.21: Normalized projection force of $N=10$ at di erent densities.

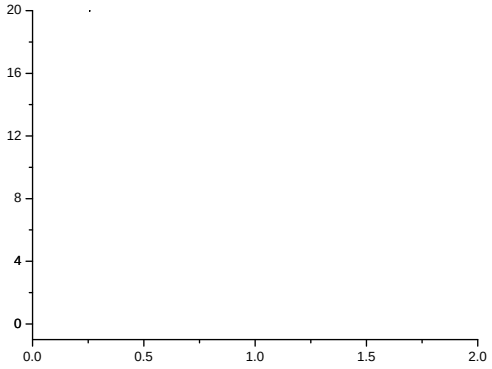

Figure 4.22: Projection force of $N=20$ at di erent densities.

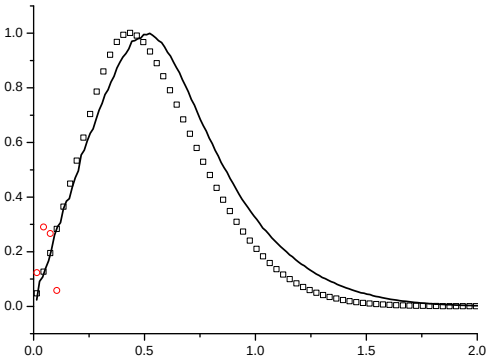

Figure 4.23: Normalized projection force of $N=20$ at di erent densities.

After normalizing these projection forces by their maximum in the system with chain length $N=10$(Fig.4.21), we can see that all results overlap with each other more or less at large distances. We suppose that the disagreement at short distances is due to the irregular shapes of two chains which are close to each other at low densities. It is clear that the force at density $= 0.05\ ^3$(red circles in Fig.4.21) is consistent with the vacuum projection force(black line in Fig.4.21). We can also see that the original projection force converges to the vacuum projection force $F_{VPF}(x)$ with decreasing density of the system(Fig.4.20). However, there is a small disagreement around $r = 1.3\sqrt{N}$ in normalized forces. We suppose this disagreement is because the chain size is slightly smaller at high densities as compared with that at lower densities due to screening of excluded volume interactions at high densities.

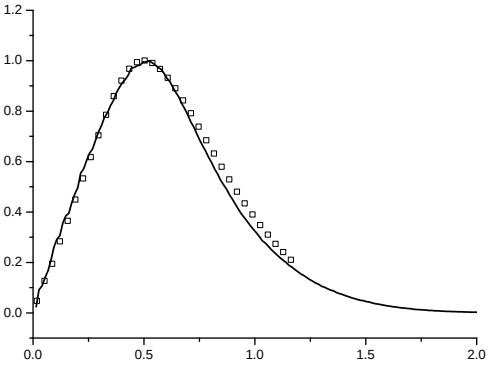

Figure 4.24: Shifted normalized projection force of $N=20$ at di erent densities.

Figure 4.25: Maximum of projection force(solid symbols) and pressure(open symbols) at di erent densities. Lines are the best t of the projection force maximum.

In the system with $N=20$, we can see that the normalized projection forces at low densities are exactly the same as the e ective force in the vacuum, but it is not true at higher densities(Fig.4.23). We suppose that the disagreement is due to the di erence of the chain size at di erent densities. After multiplying a shift factor to the x-axis, we can overlap all these forces onto the vacuum projection force(Fig.4.24). The shifting factors are 1:157 and 1:09 for $= 0:85\ ^{3}; 0:6\ ^{3}$ respectively, which are consistent with the radius of gyration of the chain at di erent densities(Fig.4.19). We can see in Fig.4.25 that the projection force maximum is proportional to the pressure at large densities. Because the chain size of $N=10$ does not heavily depend on the density of the system as the other large chain lengths, it is chosen for all the simulations in the later sections.

4.6.3 Three-body e ects in the melt

In the next two sections we investigate many-body e ects in melts.voi

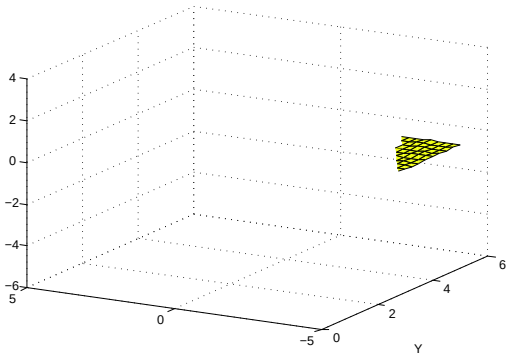

Figure 4.26: $f_{mel}(r_{12}; x_3; y_3)$ where r_{12}=0.75 .

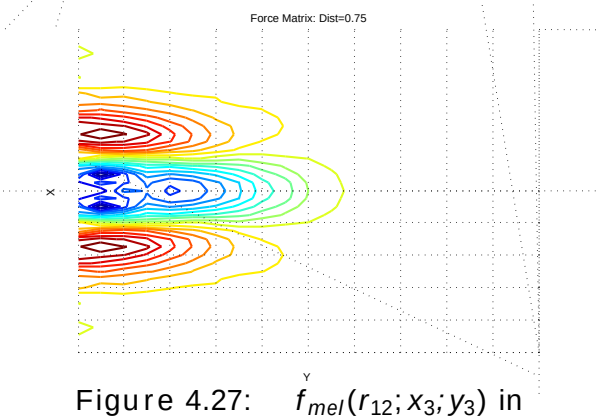

Figure 4.27: $f_{mel}(r_{12}; x_3; y_3)$ in contour where r_{12}=0.75 .

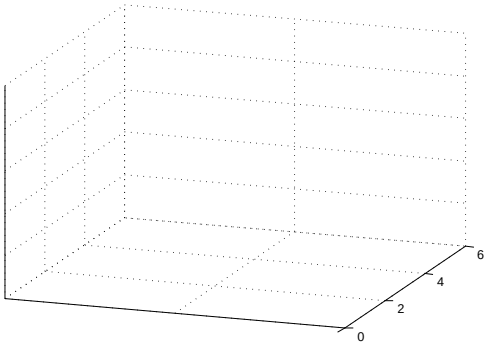

Figure 4.28: $f_{mel}(r_{12}; x_3; y_3)$ where r_{12}=1.75 .

Figure 4.29: $f_{mel}(r_{12}; x_3; y_3)$ in contour where r_{12}=1.75 .

where r_{12} is the distance between the two chains and $(x_3; y_3)$ is the relative coordinates of the third chain with respect to the center of the other two chains. The difference function $f_{mel}(r_{12}; x_3; y_3))$between between

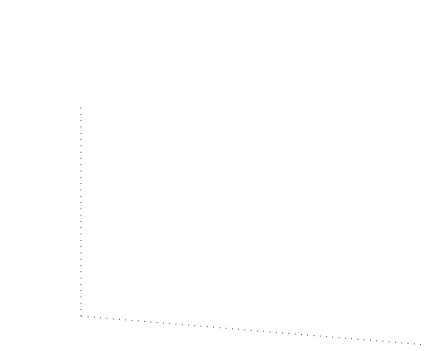

Figure 4.30: $f_{mel}(r_{12};x_3;y_3)$ where r_{12}=2.75 .

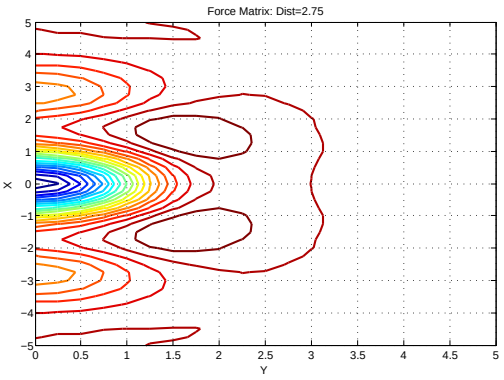

Figure 4.31: $f_{mel}(r_{12};x_3;y_3)$ in contour where r_{12}=2.75 .

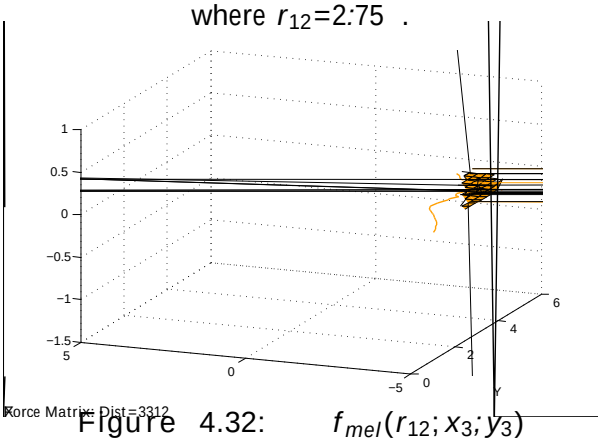

Figure 4.32: $f_{mel}(r_{12};x_3;y_3)$ where r_{12}=3.75 .

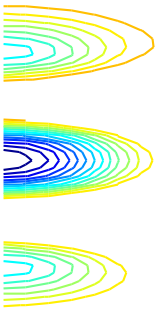

Figure 4.33: $f_{mel}(r_{12};x_3;y_3)$ in contour where r_{12}=3.75 .

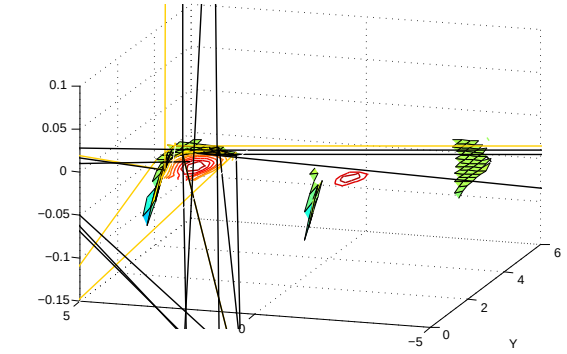

Figure 4.34: $f_{mel}(r_{12};x_3;y_3)$ where r_{12}=4.75 .

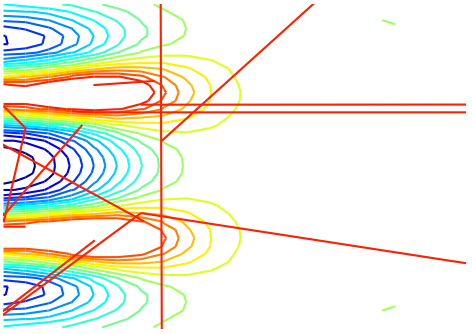

Chapter 4.

4.7 Coarse-Grained Simulations in Melts

In this section, we will test di erent pairwise interactions between blobs and then add three-body e ects into the coarse-grained simulations. The comparison of the radial distribution function of the blobs between original microscopic simulations

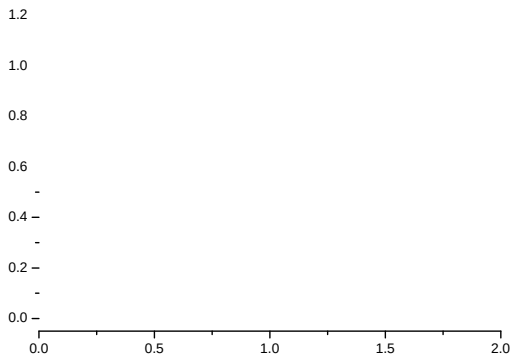

Figure 4.42: $g(r)$ from microscopic(lines) and coarse-grained(open symbols) simulations at di erent densities with N=10 by using vacuum projection force.

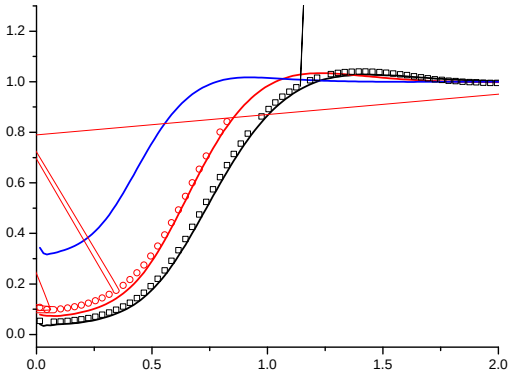

Figure 4.43: $g(r)$ from microscopic(lines) and coarse-grained(open symbols) simulations at di erent densities with N=20 by using vacuum projection force.

4.7.2 Vacuum projection force method

We use the projection force(Eq.4.9) in the vacuum from microscopic simulation to run the coarse-grained simulations at di erent densities ranging from 0:01 ^{3} to 0:85 ^{3}. Corresponding $g(r)$ are shown in Fig.4.42 and Fig.4.43. From the microscopic simulations, $g(r)$ is a monotonically increasing function at low density(black lines in Figs.4.42 and 4.43). The chains tend not to overlap with each other at short distance. The range of the correlation hole is around 1:5$^p\overline{N}$. If we increase the density of the system, $g(0)$ is not zero anymore which means that the chains start to overlap with each other and the maximum in $g(r)$ appears. The range of the correlation hole becomes smaller with increasing density. At lower densities, our vacuum projection force can reproduce $g(r)$ in coarse-grained simulations accurately, but $g(r)$ deviates from the one from microscopic simulation at high density =0:85 ^{3} as the many-body e ects start to play an important role. However, the agreement is quite good comparing to the mean eld method even at high densities(Fig.4.41).

4.7.4 Pairwise force plus three-body e ects

In this section, we will try to add many-body e ects into the coarse-grained simulations. In section 4.5.2, we showed the impact of the position of a third chain on the force between the two chains(Figs.[4.10-4.16]). We now introduce these force corrections into the coarse-grained simulations. The monomer density of the system is 0:85 ^{3}. We pre-calculate these force correction tables $f_{vac}(r_{12}; x_3; y_3)$ and $f_{mel}(r_{12}; x_3; y_3)$, where $r_{12} = \frac{i}{2}$ $\frac{1}{4}; i\ 2\ N; i\ 2$ [1; 10]. In the new coarse-grained simulations, we select all triple chains and add force corrections to every chain.

$$f_1 = f_{pair}(r_{12}) + f(r_{12}; x_3; y_3) + f_{pair}(r_{13}) + f(r_{13}; x_2; y_2) \quad (4.14)$$

$$f_2 = f_{pair}(r_{23}) + f(r_{23}; x_1; y_1) + f_{pair}(r_{21}) + f(r_{21}; x_3; y_3) \quad (4.15)$$

$$f_3 = f_{pair}(r_{31}) + f(r_{31}; x_2; y_2) + f_{pair}(r_{32}) + f(r_{32}; x_1; y_1) \quad (4.16)$$

$f(r; x; y)$ is obtained by using linear interpolation of discrete force correction tables.

$$f(r_{12}; x_3; y_3) = \frac{\frac{2i+1}{4} \quad r_{12}}{1=2} \quad f_{vac}(\frac{2i \quad 1}{4}; x_3; y_3) + \frac{r_{12} \quad \frac{2i \quad 1}{4}}{1=2} \quad f_{vac}(\frac{2i+1}{4}; x_3; y_3) \quad (4.17)$$

where $\frac{2i \quad 1}{4} \quad r_{12} \quad \frac{2i+1}{4}$.

The obtained radial distribution function $g(r)$ is shown in Fig.4.45 if the pairwise force and the three-body correction force are derived from vacuum. After introducing twice more ne-grained correction tables, we still got the same result. It shows that our correction force from the vacuum overestimates the many-body e ects.

Then we would wonder whether the prediction will be better if we use the pairwise force and three-body correction force from the melt. The results are shown in Fig.4.46, demonstrating even larger discrepancy from the microscopic simulations. As the pressure in the melt is very di erent from the one in the vacuum, we would like to erase this e ect from the melt. We have measured

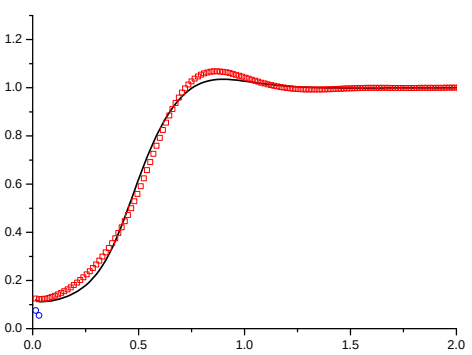

Figure 4.45: $g(r)$ in microscopic(line) and coarse-grained simulations with(blue circle) and without(red square) three-body e ects from the vaccum.

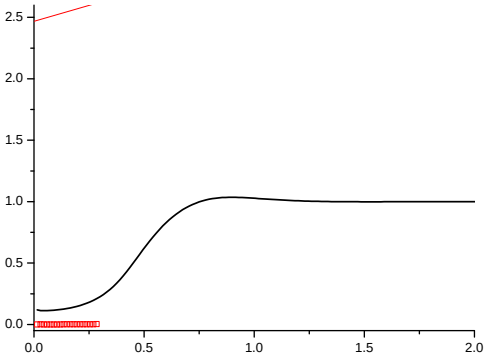

Figure 4.46: $g(r)$ in microscopic(line) and coarse-grained simulations with(blue circle) and without(red square) three-body e ect from the melt.

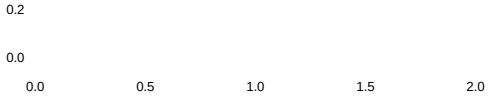

Figure 4.47: $g(r)$ in microscopic(line) and coarse-grained simulations with(blue circle) and without(red square) scaled three-body e ects from the melts.

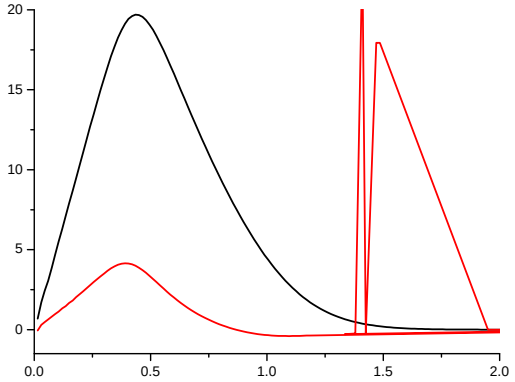

Figure 4.48: Projection force from pure repulsive Lennard-Jones potential(black line) and attractive Lennard-Jones potential(red line).

the pressure of the system at di erent densities in section 4.6.2, and derived the maximal pairwise force $f_{max}( )$ as a function of the density. The forces at high densities can be scaled down to the same amplitude of the force in vacuum. In our case the scaling ratio is chosen to be $f_{max}(0{:}01)=f_{max}$

part. The amplitude of projection force derived from this attractive system is smaller than in the purely repulsive system (Fig.4.48) and there is an attractive undershoot around $r \approx 1.0\sqrt{N}$. Furthermore $g(r)$ from both purely repulsive and attractive Lennard-Jones potentials are almost exactly the same. If we apply this force to the coarse-grained simulations, the system will be phase separated due to the attractive force.

We also applied Percus-Yevick and Hypernetted-chain closure to derive the pairwise potentials. We found that $g(r)$ in coarse-grained simulations using these potentials are exactly the same as the one from the mean field method. Derivation details are shown in Appendix B.

4.8 Conclusions

In this chapter, we have investigated the coarse-grained modelling of polymer melts. Blobs were introduced whose positions were defined as the center-of-mass of the whole chain. A procedure called force projection method was proposed to obtain the direct interaction force between the two molecules. First, we applied this method between a Rouse chain and two repulsive walls. The distribution of the chain between the walls and the force on the Rouse chain from the wall were calculated in microscopic simulations. Then we applied this force into coarse-grained simulations and obtained the same distribution function of the blobs as in the microscopic simulations, which indicates that the force projection method is a valid routine to coarse-grain the microscopic variables to mesoscopic variables. Then we replaced the Rouse chain by a single Kremer-Grest chain. The same conclusion was obtained, which means that in these simple situations the force projection method does not depend on the local structure of the chains.

Then we applied the force projection method to the two chains in vacuum to measure the direct interaction force between them as a function of their separation, which was called vacuum projection force in this thesis. This force was applied to coarse-grained simulations at different densities. $g(r)$ from these coarse-grained

Chapter 5

Conclusions

Appendix A

Normal modes

The main content in this appendix was derived in Doi and Edwards book[1]. In order to find the normal coordinates, we are using the linear transformation of $R_n(t)$

$$X_p(t) = \int_0^N {}_{pn} R_n(t) dn \tag{A.1}$$

We need to choose ${}_{pn}$ to make the equation of motion for $X_p(t)$ to have the same formula as the Ornstein-Uhlenbeck processes

$$ {}_p \frac{@X_p}{@t} = k_p X_p + f_p \tag{A.2}$$

From Eq.(1.49) and Eq.(A.2), we can see that

$$ {}_p \frac{@X_p(t)}{@t} = {}_p \int_0^N dn \; {}_{pn} @R_n t) =$$

From Eq.(A.9)

$$\begin{aligned} \langle f_p(t) f_q(0) \rangle &= \frac{p\,q}{N^2\,2} \int_0^N dn \int_0^N dm \cos\frac{p\,n}{N} \cos\frac{q\,m}{N} \langle f_n(t) f_m(0) \rangle \\ &= \frac{p\,q}{N^2\,2} \int_0^N dn \cos\frac{p\,n}{N} \cos\frac{q\,n}{N} \; 2\,k_B T \quad (t) \\ &= \frac{2}{\frac{p}{N^2\,2}}(1 + {}_{p0}) N \;{}_{pq}\; k_B T \quad (t) \end{aligned}$$

Thus the discrete and continuous normal coordinates for Rouse model are as follow:

$$X_p = \frac{1}{N+1} \sum_{i=0}^{N} R_i \cos\frac{p(i+1/2)}{N+1} \qquad (A.12)$$

$$X_p = \frac{1}{N} \int_0^N R(i) \cos\frac{pi}{N}\, di$$

$i + 1 =$

This means that the spectrum of relaxation times is given by

$$_p = \frac{_p}{k_p} = \frac{b^2}{12k_BT}\sin^{-2}\frac{p}{2(N+1)} \quad ; p = 1:::N \tag{A.18}$$

Thus, the longest relaxation time is

$$_R = {}_1 = \frac{b^2}{12k_BT}\sin^{-2}\frac{}{2(N+1)} \quad \frac{b^2(N+1)^2}{3\ ^2k_BT} \tag{A.19}$$

which is also called Rouse time.

Eq.(A.16) describes free di usion of the center of mass and N independent Ornstein-Uhlenbeck processes. The formal solution of these equations are

$$X_0(t) = X_0(0) + \frac{1}{0}\int_0^t f_0(t^0)dt^0 \tag{A.20}$$

$$= X_0(0) + \frac{1}{0}\int_0^t \sqrt{2k_BT\ _0}\,dW^0 \tag{A.21}$$

$$X_p(t) = X_p(0)\exp(-\frac{t}{p}) + \frac{1}{p}\int_0^t f_p(t^0)\exp(-\frac{t\ t^0}{p})dt^0 \tag{A.22}$$

$$= X_p(0)\exp(-\frac{t}{p}) + \frac{1}{p}\int_0^t \sqrt{2k_BT\ _p}\exp(-\frac{t\ t^0}{p})\,dW^0 \tag{A.23}$$

And we can obtain the mean-square displacement of center-of-mass and the modes correlation function as following:

$$h(X_0(t)\quad X_0(0))^2 i = \frac{2k_BT}{(N+1)}t \tag{A.24}$$

$$hX_p(t)X_q$$

Appendix B

Percus-Yevick and Hypernetted-chain closure

B.1 Ornstein-Zernike equation

In statistical mechanics the Ornstein-Zernike equation is an integral equation for de ning the direct correlation function. It basically describes how the correlations between two molecules can be calculated.

It is convenient to de ne the total correlation function:

$$h(r_{12}) = g(r_{12}) \quad 1$$

which is a measure for the \in uence" of molecule 1 on molecule 2 at distance r_{12} away with $g(r_{12})$ as the radial distribution function. In 1914 Ornstein and Zernike proposed to split this in uence into two contributions, a direct and indirect part. The direct contribution is de ned to be given by the direct correlation function, denoted $c(r_{12})$. The indirect part is due to the in uence of molecule 1 on a third molecule, labeled 3, which in turn a ects molecule 2, directly and indirectly. This indirect e ect is weighted by the density and averaged over all possible positions

of particle 3. This decomposition can written down mathematically as:

$$h(r_{12}) = c(r_{12}) + \int c(r_{13})h(r_{32})dr_3 \tag{B.1}$$

which is called Ornstein-Zernike(OZ) equation. The total correlation at r_{12} is the sum of a direct correlation plus an indirect contribution coming from all surrounding points.

Appendix B.

included, i.e. we write $g_{indirect}(r) = exp\{ (\ '(r) \ u(r))g$. Thus we can approximate $c(r)$ by

$$c(r) = e^{\ '(r)} \ e^{\ (\ '(r) \ u(r))} \tag{B.5}$$

$$u(r) = \frac{1}{} \ln \ 1 \ \frac{c(r)}{h(r) + 1} \tag{B.6}$$

which means we can obtain e ective interaction potential $u(r)$ if $h(r)$ and $c(r)$ are known.

B.3 Hypernetted-chain equation

Hypernetted-chain equation is also a closure relation to solve the Ornstein-Zernike equation which relates the direct correlation function to the total correlation function. By expanding $g_{indirect}(r)$ in the Eq.(B.5) and introducing the function

$$g(r) = h(r) + 1 = exp\{ \ '(r)g \tag{B.7}$$

we can approximate $c(r)$ by writing:

$$\begin{aligned} c(r) &= e^{\ '(r)} \ 1 + \ (\ '(r) \ u(r)) \\ &= g(r) \ 1 \ \ln g(r) \ u(r) \\ &= h(r) \ \ln g(r) \ u(r) \\ &= h(r) \ \ln(h(r) + 1) \ u(r) \end{aligned} \tag{B.8}$$

$$u(r) = \ 1) \ \ln(h(r$$

Bibliography

[1] M. Doi and S. F. Edwards. *The Theory of Polymer Dynamics*. Oxford University Press, New York, USA, 1986.

[2] M. Rubinstein and R. H. Colby. *Polymer Physics*. Oxford University Press, New York, USA, 2003.

[3] Fima C Klebaner. *Introduction to Stochastic Calculus with Applications*. Imperial College Press, London, UK, 1998.

[4] P. E. Rouse. A theory of the linear viscoelastic properties of dilute solutions of coiling polymers. *J. Chem. Phys.*, 21(7):1272{1280, 1953. doi: 10.1063/1.1699180. URL http://link.aip.org/link/?JCP/21/1272/1.

[5] G. C. Berry and T. G. Fox. *Adv. Polym. Sci.*, 5(261), 1968.

[6] R. H. Colby, L. J. Fetters, and W. W. Graessley. Melt viscosity-molecular weight relationship for linear polymers. *Macromolecules*, 20:2226{2237, 1987.

[7] P. G. de Gennes. Reptation of a polymer chain in the presence of xed obstacles. *J. Chem. Phys.*

[10] M DOI. EXPLANATION FOR THE 3.4 POWER LAW OF VISCOSITY OF POLYMERIC LIQUIDS ON THE BASIS OF THE TUBE MODEL. *JOURNAL OF POLYMER SCIENCE PART C-POLYMER LETTERS*, 19(5):265{273, 1981. ISSN 0887-6258.

[11] B. D. Todd and Peter J. Daivis. Homogeneous non-equilibrium molecular dynamics simulations of viscous ow: techniques and applications. *MOLECULAR SIMULATION*, 33(3):189{229, 2007. ISSN 0892-7022. doi: *f*10.1080/08927020601026629*g*.

[12] Kurt Kremer and Gary S. Grest. Dynamics of entangled linear polymer melts: A molecular-dynamics simulation. *J. Chem. Phys.*, 92(8):5057{5086, 1990. doi: 10.1063/1.458541. URL http://link.aip.org/link/?JCP/92/5057/1.

[13] Rolf Auhl, Ralf Everaers, Gary S. Grest, Kurt Kremer, and Steven J. Plimpton. Equilibration of long chain polymer melts in computer simulations. *J. Chem. Phys.*, 119(24):12718{12728, 2003. doi: 10.1063/1.1628670. URL http://link.aip.org/link/?JCP/119/12718/1.

[14] P. G. de Gennes. *Scaling Concepts in Polymer Physics*. Cornell University Press, 1979.

[15] M DOI. EXPLANATION FOR THE 3.4-POWER LAW FOR VISCOSITY OF POLYMERIC LIQUIDS ON THE BASIS OF THE TUBE MODEL. *JOURNAL OF POLYMER SCIENCE PART B-POLYMER PHYSICS*, 21 (5):667{684, 1983. ISSN 0887-6266.

[16] M. Rubinstein and R. H. Colby. Self-consistent theory of polydisperse entangled polymers: Linear viscoelasticity of binary blends. *J. Chem. Phys.*, 89: 5291{5306, 1988.

[17] A. E. Likhtman and T. C. B. McLeish. Quantitative theory for linear dynamics of linear entangled polymers. *Macromolecules*, 35:6332{6343, 2002.

[18] Alexei E. Likhtman. Single-chain slip-link model of entangled polymers: Simultaneous description of neutron spin-echo, rheology, and di usion. *Macromolecules*, 38(14):6128{6139, 2005. doi: 10.1021/ma050399h. URL http://pubs.acs.org/doi/abs/10.1021/ma050399h.

[19] R. C. Ball and T. C. B. McLeish. Dynamic dilution and the viscosity of star polymer melts. *Macromolecules*, 22:1911{1913, 1989.

[20] ST Milner and TCB McLeish. Arm-length dependence of stress relaxation in star polymer melts. *MACROMOLECULES*, 31(21):7479{7482, OCT 20 1998. ISSN 0024-9297.

[21] G MARRUCCI. RELAXATION BY REPTATION AND TUBE ENLARGEMENT - A MODEL FOR POLYDISPERSE POLYMERS. *JOURNAL OF POLYMER SCIENCE PART B-POLYMER PHYSICS*, 23(1):159{177, 1985. ISSN 0887-6266.

[22] M DOI, WW GRAESSLEY, E HELFAND, and DS PEARSON. DYNAMICS OF POLYMERS IN POLYDISPERSE MELTS. *MACROMOLECULES*, 20 (8):1900{1906, AUG 1987. ISSN 0024-9297.

[23] M. J. Struglinski and W. W. Graessley. E ects of polydispersity on the linear

[26] S. Wang, S.-Q. Wang, A. Halasa, and W.-L. Hsu. Relaxation dynamics in mixtures of long and short chains: Tube dilation and impeded curvilinear di usion. *Macromolecules*, 36:5355{5371, 2003.

[27] JL VIOVY, M RUBINSTEIN, and RH COLBY. CONSTRAINT RELEASE IN POLYMER MELTS - TUBE REORGANIZATION VERSUS TUBE DILATION. *MACROMOLECULES*, 24(12):3587{3596, JUN 10 1991. ISSN 0024-9297.

[28] Zuowei Wang and Ronald G. Larson. Constraint release in entangled binary blends of linear polymers: A molecular dynamics study. *MACROMOLECULES*, 41(13):4945{4960, JUL 8 2008. ISSN 0024-9297. doi: *f*10.1021/ma800680b*g*.

[29] Jorge Ramirez, Sathish K. Sukumaran, Bart Vorselaars, and Alexei E. Likhtman. E cient on the y calculation of time correlation functions in computer simulations. *JOURNAL OF CHEMICAL PHYSICS*, 133(15), OCT 21 2010. ISSN 0021-9606. doi: *f*10.1063/1.3491098*g*.

[30] Alexei E. Likhtman, Sathish K. Sukumaran, and Jorge Ramirez. Linear viscoelasticity from molecular dynamics simulation of entangled polymers. *Macromolecules*, 40(18):6748{6757, 2007. doi: 10.1021/ma070843b. URL http://pubs.acs.org/doi/abs/10.1021/ma070843b.

[31] C. M. Ylitalo, J. A. Korn eld, G. G. Fuller, and Dale S. Pearson. Molecular weight dependence of component dynamics in bidisperse melt rheology. *Macromolecules*, 24(3):749{758, 1991. doi: 10.1021/ma00003a019. URL http://pubs.acs.org/doi/abs/10.1021/ma00003a019.

[32] Jorge Ram rez, Sathish K. Sukumaran, and Alexei E. Likhtman. Signi cance of cross correlations in the stress relaxation of polymer melts. *J. Chem. Phys.*, 126(24):244904, 2007. doi: 10.1063/1.2746867. URL http://link.aip.org/link/?JCP/126/244904/1.

[33] M. Doi, D. Pearson, J. Korn eld, and G. Fuller. E ect of nematic interaction in the orientational relaxation of polymer melts. *Macromolecules*, 22(3):1488{1490, 1989. doi: 10.1021/ma00193a082. URL http://pubs.acs.org/doi/abs/10.1021/ma00193a082.

[34] M. Doi and H. Watanabe. E ect of nematic interaction on the rouse dynamics. *Macromolecules*, 24(3):740{744, 1991. ISSN 0024-9297. doi: 10.1021/ma00003a017. URL http://dx.doi.org/10.1021/ma00003a017.

[35] R. Graf, A. Heuer, and H. W. Spiess. Chain-order e ects in polymer melts probed by *h*1 double-quantum nmr spectroscopy. *Phys. Rev. Lett.*, 80(26):5738{5741, 1998. doi: 10.1103/PhysRevLett.80.5738.

[36] A. R. C. Baljon, G. S. Grest, and T. A. Witten. Simulations of induced orientation in stretched polymer melts. *Macromolecules*, 28(6):1835{1840, 1995. doi: 10.1021/ma00110a017. URL http://pubs.acs.org/doi/abs/10.1021/ma00110a017.

[37] J. M. Deutsch and J. H. Pixley. Induced orientational e ects in relaxation of polymer melts. *Phys. Rev. E*, 80(1):011803, Jul 2009. doi: 10.1103/PhysRevE.80.011803.

[38] H. Watanabe. Viscoelasticity and dynamics of entangled polymers. *Prog. Polym. Sci.*

[48] D PEARSON, E HERBOLZHEIMER, N GRIZZUTI, and G MARRUCCI. TRANSIENT-BEHAVIOR OF ENTANGLED POLYMERS AT HIGH SHEAR RATES. *JOURNAL OF POLYMER SCIENCE PART B-POLYMER PHYSICS*, 29(13):1589{1597, DEC 1991. ISSN 0887-6266.

[49] DW MEAD and LG LEAL. THE REPTATION MODEL WITH SEGMENTAL STRETCH .1. BASIC EQUATIONS AND GENERAL-PROPERTIES. *RHEOLOGICA ACTA*, 34(4):339{359, JUL-AUG 1995. ISSN 0035-4511.

[50] A.W Lees and S.F Edwards. The computer study of transport processes under extreme conditions. *J. Phys. C*, 5:1921, 1972.

[51] WG HOOVER, DJ EVANS, RB HICKMAN, AJC LADD, WT ASHURST, and B MORAN. LENNARD-JONES TRIPLE-POINT BULK AND SHEAR VISCOSITIES - GREEN-KUBO THEORY, HAMILTONIAN-MECHANICS, AND NON-EQUILIBRIUM MOOY 690YNAMICS. *PHYSICAL REVIEW A*, 22(4):1690{1697, 1980. ISSN 1050-2947.

[52] Denis J. EvSDSE5s.

[56] H. C. Andersen. Molecular dynamics simulations at constant pressure and/or temperature. *J. Chem. Phys.*, 72(4):2384{2393, 1980. doi: 10.1063/1.439486. URL http://link.aip.org/link/?JCP/72/2384/1.

[57] P ESPANOL and P WARREN. STATISTICAL-MECHANICS OF DISSIPATIVE PARTICLE DYNAMICS. *EUROPHYSICS LETTERS*, 30(4):191{196, MAY 1 1995. ISSN 0295-5075.

[58] EV MENEZES and WW GRAESSLEY. NON-LINEAR RHEOLOGICAL BEHAVIOR OF POLYMER SYSTEMS FOR SEVERAL SHEAR-FLOW HISTORIES. *JOURNAL OF POLYMER SCIENCE PART B-POLYMER PHYSICS*, 20(10):1817{1833, 1982. ISSN 0887-6266.

[59] T Schweizer, J van Meerveld, and HC Ottinger. Nonlinear shear rheology of polystyrene melt with narrow molecular weight distribution - Experiment and theory. *JOURNAL OF RHEOLOGY*, 48(6):1345{1363, NOV-DEC 2004. ISSN 0148-6055. doi: *f*10.1122/1.1803577*g*.

[60] Rodrigo E. Teixeira, Hazen P. Babcock, Eric S. G. Shaqfeh, and Steven Chu. Shear thinning and tumbling dynamics of single polymers in the ow-gradient plane. *Macromolecules*, 38(2):581{592, 2005. doi: 10.1021/ma048077l. URL http://pubs.acs.org/doi/abs/10.1021/ma048077l.

[61] Pouyan E. Boukany, Orin Hemminger, Shi-Qing Wang, and L. J. Lee. Molecular Imaging of Slip in Entangled DNA Solution. *PHYSICAL REVIEW LETTERS*, 105(2), JUL 9 2010. ISSN 0031-9007. doi: *f*10.1103/PhysRevLett.105.027802*g*.

[62] Richard S. Graham, Alexei E. Likhtman, Tom C. B. McLeish, and Scott T. Milner. Microscopic theory of linear, entangled polymer chains under rapid deformation including chain stretch and convective constraint release. *J. Rheol.*, 47(5):1171{1200, 2003. doi: 10.1122/1.1595099. URL http://link.aip.org/link/?JOR/47/1171/1.

[63] Dietmar Auhl, Jorge Ramirez, Alexei E. Likhtman, Pierre Chambon, and Christine Fernyhough. Linear and nonlinear shear ow behavior of monodisperse polyisoprene melts with a large range of molecular weights. *JOURNAL OF RHEOLOGY*, 52(3):801{835, MAY-JUN 2008. ISSN 0148-6055. doi: *f*10.1122/1.2890780*g*.

[64] P Espanol, M Serrano, and I Zuniga. Coarse-graining of a uid and its relation with dissipative particle dynamics and smoothed particle dynamics. *INTERNATIONAL JOURNAL OF MODERN PHYSICS C*, 8(4):899{908, AUG 1997. ISSN 0129-1831. 6th International Conference on Discrete Models for Fluid Mechanics, BOSTON, MA, AUG 26-28, 1996.

[65] AK Soper. Empirical potential Monte Carlo simulation of uid structure. *CHEMICAL PHYSICS*, 202(2-3):295{306, JAN 15 1996. ISSN 0301-0104.

[66] D LEVESQUE, JJ WEIS, and L REATTO. PAIR INTERACTION FROM STRUCTURAL DATA FOR DENSE CLASSICAL LIQUIDS. *PHYSICAL REVIEW LETTERS*, 54(5):451{454, 1985. ISSN 0031-9007.

[67] CD BERWEGER, WF VANGUNSTEREN, and F MULLERPLATHE. FORCE-FIELD PARAMETRIZATION BY WEAK-COUPLING - REENGINEERING SPC WATER. *CHEMICAL PHYSICS LETTERS*, 232(5-6):429{436, JAN 27 1995. ISSN 0009-2614.

[68] Reinier L. C. Akkermans and W. J. Briels. A structure-based coarse-grained model for polymer melts. *J. Chem. Phys.*, 114(2):1020{1031, 2001. doi: 10.1063/1.1330744. URL http://link.aip.org/link/?JCP/114/1020/1.

[69] Reinier L. C. Akkermans and W. J. Briels. Coarse-grained dynamics of one chain in a polymer melt. *J. Chem. Phys.*, 113(15):6409{6422, 2000. doi: 10.1063/1.1308513. URL http://link.aip.org/link/?JCP/113/6409/1.

[70]